ABSTRACT

SIEGEL, CAMERON ANDREW. Geomorphic Analysis of a Transitional Landscape at the Colorado River and Great Basin Boundary, Southeastern Nevada. Under the direction of Dr. Magdalena Ellis Curry.

Despite confining the timing of the Lower Colorado River's development through the Lake Mead area in Southeastern Nevada to about 5.6 Ma, the river's effects on the regional inherited topography remain unclear. In this contribution, we use computational topographic analyses to investigate an erosional response to increased stream power driven by the arrival of the lower Colorado River in southern Nevada and its role in shaping the modern catchment. The Lower Colorado River catchment has a unique morphology extending north from Lake Mead, splitting into three elongated channels, two of which follow Basin and Range topography: the White River Valley and the Meadow Valley Wash. Both channels show evidence of basin capture events that have enlarged the watersheds, but the timing of these captures is loosely constrained.

We conducted a geomorphic study using a Chi (χ) analysis of stream channels, knickpoint celerity modeling, and cosmogenic catchment-averaged erosion rates. Using a 30-meter DEM and TopoToolbox MATLAB scripts, we identified a suite of regional knickpoints within elevations of ~675-850 m, including two knickpoints in the main drainage channels at ~800 m. The knickpoint celerity model, employing a grid search approach testing erodibility values between 1×10^{-11} to 1×10^{-13} ms^2kg^{-1} for two lithologies, shows that it is possible for the stream to erode to the location of the ~800 m knickpoints over 5.6 m.y. Modern fluvial sediment samples from the Meadow Valley Wash yielded catchment-average erosion rates between 19.6 and 54.8 mm/k.y.

Knickpoints were identified in the Miocene to Holocene aged basin fill strata of the Meadow Valley Wash and White River Valley, however, their distribution in χ vs. elevation space suggests no genetic relationship, potentially due to basin capture events along the channel during knickpoint propagation. Our modeling of knickpoint propagation up the catchment may have overestimated erodibility, suggesting difficulty for knickpoints to propagate far up the catchment, however, the Plio-Pleistocene wetter-than-modern climate in our study area suggests knickpoint propagation may have been faster than modeled. The catchment-averaged erosion rates are comparable to other arid regions, but the channel steepness is unusually high, likely due to basin integration events.

Our evidence supports the hypothesis that the modern catchment resulted from a combination of basin spill-over from endorheic basins and higher-than-modern channel head erosion from the Lower Colorado River's side of the drainage divide. We suggest future work should focus on tephrostratigraphic studies within formerly endorheic basins to constrain better the timing of basin integration and landscape evolution models that consider lithologic changes, past precipitation variations, and basin integrations. Such studies will enhance the understanding of landscape evolution in Southeastern Nevada and the drainage divide history between the Lower Colorado River catchment and the Great Basin.

Geomorphic Analysis of a Transitional Landscape at the Colorado River and Great Basin Boundary, Southeastern Nevada.

by
Cameron Andrew Siegel

A thesis submitted to the Graduate Faculty of
North Carolina State University
in partial fulfillment of the
requirements for the degree of
Master of Science

Marine, Earth, and Atmospheric Sciences

Raleigh, North Carolina
2024

APPROVED BY:

_____	_____
Dr. Magdalena Ellis Curry Committee Chair	Dr. Karl Wegmann
_____	
Dr. DelWayne Bohnenstiehl	

BIOGRAPHY

Cameron was born in Burlington, Vermont, at the foot of the mighty Green Mountains, and spent his first 3 years living in Charlotte, Vermont. For the rest of his youth, Cameron grew up in Annapolis, Maryland. Being surrounded by the Chesapeake Bay sparked his interest in environmental change and earth systems sciences. He earned his Bachelor of Arts degree in Geosciences from Franklin & Marshall College in Lancaster, Pennsylvania. While attending Franklin & Marshall College he gained research experience in geomorphology under the guidance of Dr. Dorothy Merritts. Cameron conducted his M.S. at North Carolina State University under the guidance and advisement of Dr. Magdalena Ellis Curry.

ACKNOWLEDGMENTS

Firstly, I would like to express my deepest gratitude to Dr. Magdalena Ellis Curry. Thank you for giving me the opportunity to come to NCSU and for working with me to develop my research project. Your kindness, guidance, and support have been pivotal in conducting my research and achieving success in this program.

I would also like to thank my committee members, DelWayne Bohnenstiehl and Karl Wegmann, for their valuable input and support. A special thanks to Karl Wegmann for always being willing to take a tangent. Del you are also pretty funny guy.

I am grateful to the faculty and staff in the Department of Earth and Environment at Franklin & Marshall College for their fantastic teaching, research, and field opportunities, which inspired me to pursue geologic research.

To the graduate students in the Department of Marine, Earth and Atmospheric Sciences: thank you for your support and friendship. I am fortunate to have found such a friendly and welcoming graduate department. Thank you to my friends who constantly encouraged me when I doubted myself and helped me stay on track.

Special thanks to my lab mates, Trevor Gunn and Kris Symanski, for your support, friendship, and banter.

I would also like to thank the students I have had the pleasure of TAing, both in the classroom and in the field. Teaching has given me new perspectives on science communication and understanding geologic principles.

Lastly, I would like to thank my parents and brother for their unwavering support and encouragement throughout my academic journey.

TABLE OF CONTENTS

LIST OF TABLES

LIST OF FIGURES

INTRODUCTION

Southeastern Nevada provides a window into the interplay between the externally drained catchment of the lower Colorado River (LCR) and the endorheic (internally drained) Great Basin catchment system. The modern landscape has been shaped by three major tectonic events over the last 160 m.y., including the Sevier orogeny, Cenozoic ignimbrites, and Basin and Range extension (Armstrong, 1968; Best et al., 2013a; Yonkee and Weil, 2015; Rowley et al., 2017).

The modern catchment of the LCR has a unique morphology resulting from the integration of previously endorheic basins. The present chronology of three basin integration events along the modern Meadow Valley Wash (MVW) and White River Valley (WRV) (Figure 1) has been loosely constrained through the analysis of incised basin-fill sedimentary deposits. Evidence of a transition to external drainage is present with the deposition of coarse and poorly sorted higher-energy fluvial gravels over fine-grained lacustrine sandstone (Diguiseppi and Bartley, 1991; Pederson, 1999). The perched Panaca basin lying along the MVW (within the Caliente and Indian Peak Caldera Complexes) and the northern basin in the WRV are both interpreted to have integrated into the LCR catchment during the Pleistocene (Figure 1) (Diguiseppi and Bartley, 1991; Pederson et al., 2000). The Glendale Basin, at the confluence of the MVW and WRV, is believed to have been incorporated into the LCR catchment after 3 Ma based on tephrostratigraphy of the Upper Horse Hills Ash (Figure 1) (Pederson, 1999; Pederson et al., 2000; Dickinson et al., 2014).

The capture of endorheic basins has been discussed extensively with three main proposed mechanisms for their integration: 1) bottom-up integration whereby channel head erosion from an adjacent basin migrates upward, first capturing the groundwater drainage divide and ultimately breaching the topographic drainage divide into the internally drained basin; 2) top-

down integration whereby endorheic basins fill with sediment and water and spill over the drainage divide, cutting through and connecting the two basins; and 3) a combination of mechanisms 1 and 2 (Pederson, 2008; Meek, 2019; Hilgendorf et al., 2020; Larson et al., 2022). Meek (2019) proposed mechanism 2 (top-down) for integration of the MVW's Panaca basin into the LCR catchment due to the arid climate not supporting intense channel head erosion from the LCR side of the drainage divide. Conversely, Pederson (2008) suggests that mechanism 3 (both bottom-up and top-down), with the influence of groundwater sapping, is the likely force behind the formation of the modern catchment. Recent work from Faulds et al. (2016) established the LCR as a through-flowing river through the modern Lake Mead region ca. 5.6 Ma. However, the effect on the inherited catchment's landscape from this massive increase in stream power and local base-level incision has yet to be assessed.

It is well-established that bedrock river systems preserve evidence of perturbation events such as base-level fall and basin capture (Merritts and Vincent, 1989; Pazzaglia et al., 1998; Whipple and Tucker, 1999; Snyder et al., 2000; Willett et al., 2014). The further development and application of topographic analysis techniques on bedrock rivers for the preserved evidence of these perturbation events has been extensively demonstrated in the literature (Whittaker and Boulton, 2012; Kirby and Whipple, 2012; Gallen et al., 2013; Perron and Royden, 2013; Yanites et al., 2013; Willett et al., 2014; Gallen and Wegmann, 2017, etc).

In this contribution, we test the hypothesis that an erosional response caused by the increase in stream power at the base level of the local catchment starting at 5.6 Ma may have contributed to the capture of endorheic basins that were once part of the Great Basin catchment system via mechanism 1, bottom-up basin integration. We conduct a multifaceted study incorporating topographic analysis for preserved evidence of a base-level fall event, modeling

bottom-up erosion through the WRV and MVW, and assessing modern catchment basin-average erosion rates.

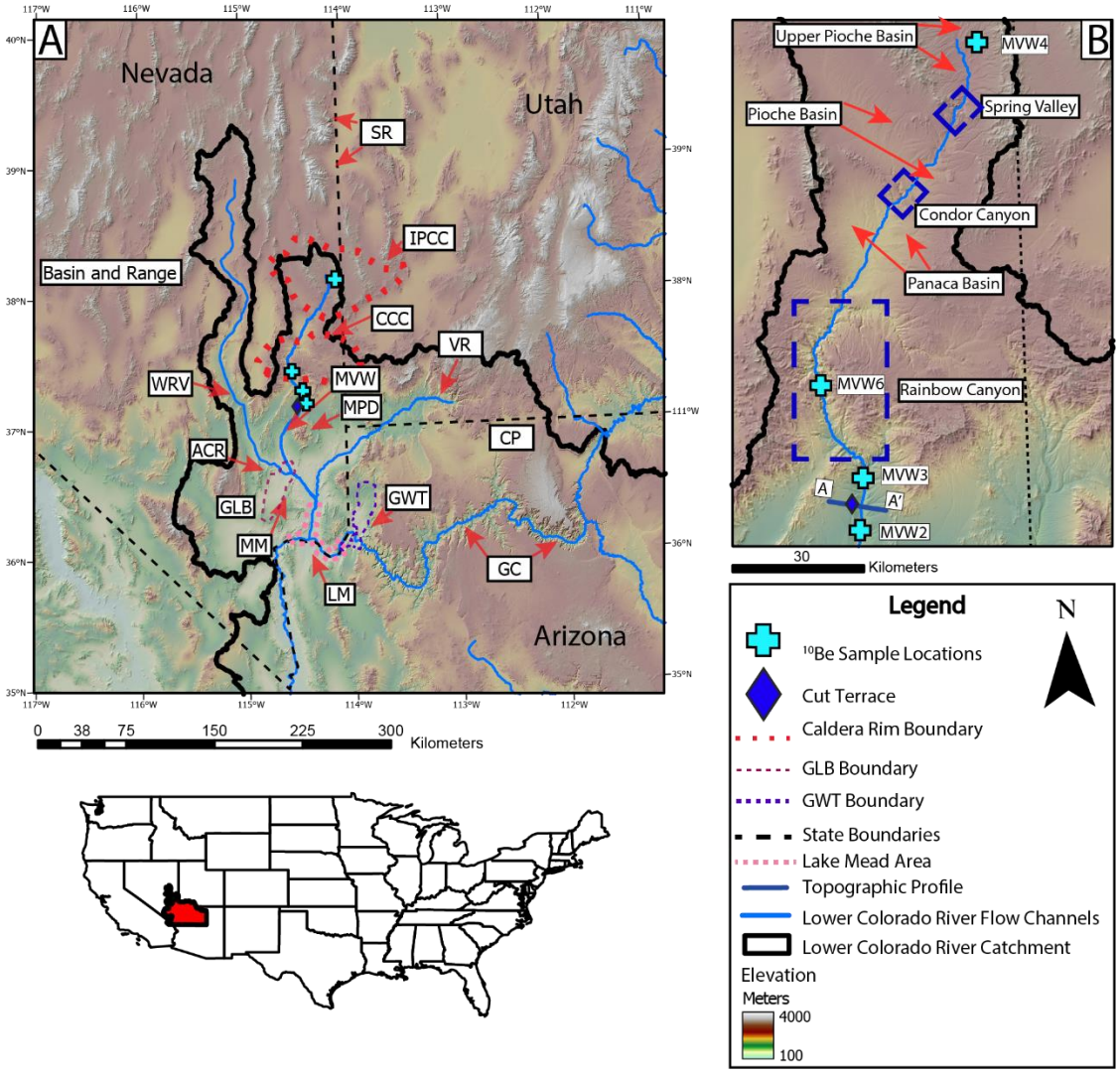

Figure 1. The elevation map of the study area. GB - Great Basin Watershed; SR - Snake Range; MPD - Mormon Peak Detachment; CP - Colorado Plateau; GC - Grand Canyon; WRV - White River Valley; MVW - Meadow Valley Wash; MM – Muddy Mountains; GLB – Glendale basin; ACR – Arrow Canyon Range; VR – Virgin River; GWT - Grand Wash Trough; CCC - Caliente Caldera Complex; IPCC – Indian Peak Caldera Complex; LM – Lake Mead Area. Red polygon on the USA map represents the LCR catchment extent shown in A.

GEOLOGIC SETTING

Tectonic History

The study area lies within the lower Colorado River (LCR) drainage basin in southeastern Nevada, including its drainage divide with the endorheic Great Basin (Figure 1). The ultimate base level for the LCR drainage basin is the Gulf of California. However, within the context of this study, the local base level is modern Lake Mead, west of where the Colorado River exits the Grand Canyon and enters the Basin and Range province. Three major tectonic and volcanic events are superimposed within the study area: the Sevier orogeny, Cenozoic ignimbrites, and Basin and Range extension. From the middle Triassic to the early Cenozoic the Sevier orogeny affected much of the American Cordillera when the Farallon plate subducted under the North American plate. This orogeny produced a north-northeast striking fold-thrust belt that placed Neoproterozoic to middle Paleozoic rocks on top of Paleozoic to Jurassic units (Armstrong, 1968; Yonkee and Weil, 2015; Rowley et al., 2017). Across the study area, the majority of these rocks are carbonate and some clastic deep marine Paleozoic rocks (Rowley et al., 2017).

In the mid-Cenozoic, delamination of the Farallon plate caused mantle upwelling and subsequent volcanism (Best et al., 2016). This major ignimbrite flare-up encompassed western Utah and Nevada, comprising the Indian Peak-Caliente Caldera Complex (CC), the Central Nevada CC, and the Western Nevada CC (Best et al., 2016). These three ignimbrite provinces stretch from the eastern edge of the Sierra Nevada to the Sevier fold-thrust belt and resulted in high topography across the modern Basin and Range region known as the “Nevadaplano” (DeCelles, 2004; Rowley et al., 2017). In the study area, the Indian Peak-Caliente CC is responsible for relief generation, geodynamic uplift, and copious volcanic material overlying the Sevier Orogeny fold-thrust belt. The Indian Peak-Caliente CC was active between 36 and 18 Ma,

producing an estimated 33,000 km^2 of material and high topography with thick caldera rims (Best et al., 1989, 2013a, 2013b, 2016).

In eastern Nevada the onset of Basin and Range east-west oriented extension was ca. 20 Ma; however, most of the modern Basin and Range topography in the study area formed during a main phase of extension ca. 17 to 12 Ma and after 10 Ma (Rowley et al., 1981, 2017; Liberty et al., 1994). To the north of the study area, the Snake Range experienced 12-15 km of extension ca. 17 Ma (Miller et al., 1999). To the south of the study area, the Mormon Peak Detachment experienced 10.9 to 19.5 km of extension ca. 14-13 Ma (Bidgoli et al., 2015). Other minor normal faults distributed within the study area disrupt local drainage basin geometries. Basin and Range extension established regional drainage patterns leading to individual, internally-drained (endorheic) basins, some of which were formed in the highly elevated topography created by Cenozoic volcanism and the Sevier Orogeny.

Drainage Basin Reorganization and Geomorphology

The isolated basins that formed in the hanging walls of major Basin and Range structures in SE Nevada were loci for a series of freshwater lakes and playas that most likely began to be filled towards the end of extension through the Pleistocene due to the development of a wet climate in Nevada and the western USA (Ibarra et al., 2018; Abell et al., 2021). These lakes were fed by water from their localized catchments and likely groundwater-fed from the Colorado Plateau (Faulds et al., 2016). The lakes deposited thick units (200-2,500 m) of evaporite such as gypsum and halite or freshwater carbonate (Faulds et al., 2016). The Colorado River began to flow into this internal lake system via a series of east-to-west basin spillover events beginning in the Grand Wash Trough (Figure 1) around 12 Ma and progressing into the Lake Mead area ca. 10 Ma. Based on Sr isotope data, the development of a throughgoing Lower Colorado River in

the Las Vegas area occurred ca. 5.6 Ma (Roskowski et al., 2010; Spencer et al., 2013; Faulds et al., 2016), reaching the proto-Gulf of California between 4.8 and 4.63 Ma (Crow et al., 2021).

The segment of the LCR in our study area flows through modern Lake Mead and incorporates six basins in its northern catchment. There are four basins along the MVW, all connected by incised canyons (from the highest elevated basin to the lowest): the upper Pioche, the Pioche, the Panaca, and the MVW (Fig. 1). These are connected by the Spring Valley, Condor, and Rainbow Canyons respectively. It has been suggested that the progressive interconnectedness of the Pioche and Panaca basins is due to the spillover of these formerly internally drained basins (Meek, 2019). The previously internally drained basins contain thick sedimentary basin fill deposits that transition up-section where an unconformity separates fine-grained sandstone and coarse fluvial gravels, which has been interpreted as evidence of a change from an endorheic to an externally drained basin. The main basin fill unit of the Panaca Basin is the Panaca Formation; based on well data, it is estimated to be a minimum of 425 m thick (Phoenix, 1948). Ash-flow tuff deposits at the base of an exposed portion of the Panaca formation were geochemically correlated to ash deposits dated 4.64 +/- 0.03 Ma (Pederson, 1999). An ash layer in the upper portion of the Panaca Formation was geochemically correlated to the Huckleberry Ridge ash, which is 2.09 +/- 0.009 Ma (Sarna-Wojcicki, personal comm. to (Pederson, 1999)). These ash correlations suggest that the Panaca Basin was likely integrated into the LCR catchment in the Pleistocene (Pederson, 1999; Pederson et al., 2000). Prominent cut terraces in the basin fill deposits of the MVW lie just south of the rim of the Caliente Caldera complex. A cross-section across the basin (Figure 2) shows evidence of a paleo-valley bottom that was incised over 250 meters to form the modern drainage of the MVW. The ages of fill deposition and incision into this terrace are unknown. To the west of the Panaca Basin and just

west of the Caliente Caldera Complex, the stratigraphy in the WRV shows evidence for the integration of an internally drained basin into the LCR catchment. Alluvial plain and fluvial terrace deposits lie unconformably on top of the White River Narrows formation (an endorheic basin fill unit). Based on these stratigraphic observations, the upper basin in the WRV is interpreted to have been incorporated into the LCR drainage basin in the late Pleistocene (Diguiseppi and Bartley, 1991). The Glendale basin lies northwest of the Muddy Mountains (Figure 1) and at the confluence of the WRV and MVW containing the thoroughly studied Muddy Creek formation. Analysis of the Muddy Creek Formation has led to an interpretation that it was integrated into the LCR catchment sometime after 3 Ma based on an ash bed found within the Muddy Creek formation chemically correlated to the Upper Horse Hill Ash (Williams, 1994; Pederson, 1999; Pederson et al., 2001; Dickinson et al., 2014).

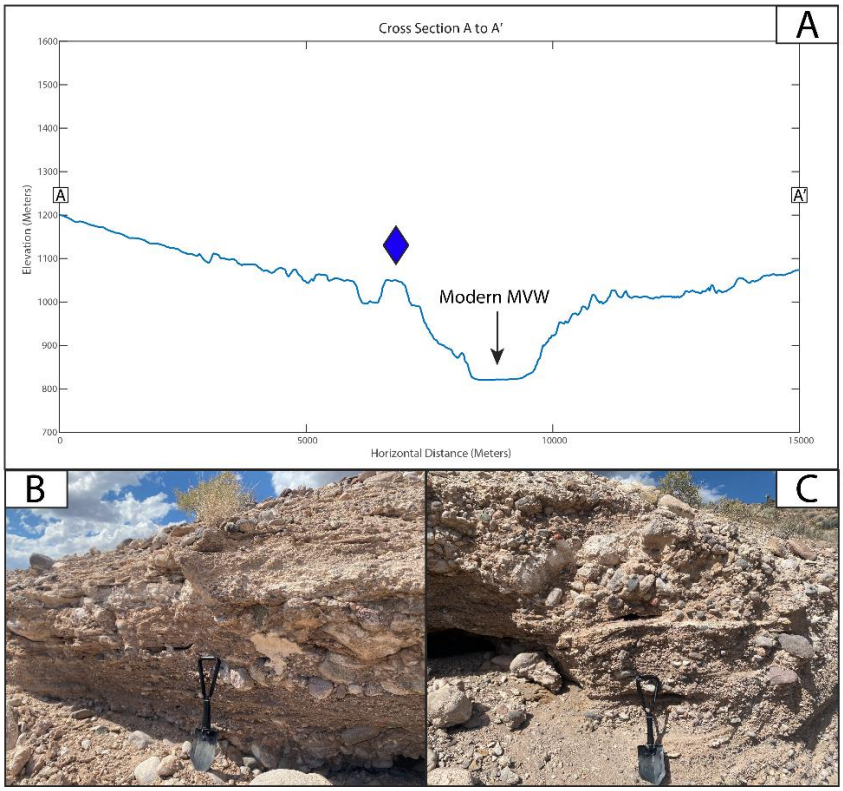

Figure 2. A) Topographic profile across the Meadow Valley Wash at location A-A' in Figure 1. B) Exposure of the upper meters of the terrace fill deposit is located at the blue diamond. C) The same exposure as in B from a different view angle. Note the stratified, coarse fluvial gravel deposit characteristic of large alluvial fans or powerful streams.

METHODOLOGY

We use three computational methods to assess the landscape evolution of the LCR drainage basins in the Meadow Valley Wash and White River Valley, which will give insight into the drainage basin and fluvial history of the LCR watershed.

River profile analysis

Analyzing stream channel gradients is a proven technique to give insight into the erosion and uplift of drainage networks in equilibrium systems where uplift equals erosion and transient systems where the landscape is responding to a tectonic forcing and/or base level fall (e.g., Harkins et al., 2007; Kirby and Whipple, 2012; Gallen and Wegmann, 2017). In an idealized equilibrium scenario, bedrock lithology, climate, and uplift are spatially and temporally constant along the longitudinal profile of a river channel. The relationship between the change in stream channel elevation (*dz*) over time (*dt*) in a detachment-limited system (i.e., where erosion is limited by the ability of the stream to detach bedrock) is represented by the steam power incision law (Howard, 1994):

$$\frac{dz}{dt} = U - E = U - KA^m S^n \quad (1)$$

Where U and E are uplift and erosion respectively; K is erodibility ($L^{1-2m}\,t^{-1}$) that is dependent on lithology, climate, and other factors; A is upstream drainage area, S is channel slope, m and n are erosional constants based on channel morphology (Whipple and Tucker, 1999; Whipple, 2004). A system is considered to be in a steady state when uplift and erosion rates are equal. Given a steady state system, S can be determined by Flint's Law:

$$S = K_s A^{-\theta} \quad (2)$$

Where A is the upstream drainage area, K_s represents the channel steepness index at a point along the profile, and θ is the basin concavity index (Flint, 1974; Snyder et al., 2000). Rearranging the steam power incision law (equation 1) results in a power-law relationship between slope and drainage area in a similar form to equation 2:

$$S = \left(\frac{U}{K}\right)^{\frac{1}{n}} A^{-\left(\frac{m}{n}\right)} \quad (3)$$

Equation 3 predicts that slope is dependent basin area and uplift rate(s). Equation 2 is ideal for analyzing drainage basins because K_s and θ can be calculated via linear regression of slope and drainage area on a log-log plot (Kirby and Whipple, 2012). Equation 3 shows that K_s and θ fluctuate together in different catchments based on the channel morphology constant n (Snyder et al., 2000; Wobus et al., 2006; Kirby and Whipple, 2012), therefore a reference concavity is used to compare K_s across drainages/basins. Substituting a commonly used reference concavity for θ in equation 2 creates the metric, normalized channel steepness (K_{sn}). We use a reference concavity of 0.45 (Snyder et al., 2000; Wobus et al., 2006; Kirby and Whipple, 2012).

When a steady-state system experiences a fall in base level, the ensuing disequilibrium can create a wave of increased channel erosion starting at the mouth of the channel. This erosional wave represents a knickpoint (a break in channel steepness from high to low) separating the recently incised lower segment from the remnant upper section of the channel. (Whittaker and Boulton, 2012). The integral metric Chi (χ) is used often in the topographic analysis of a catchment system (Perron and Royden, 2013):

$$\chi = \int_{x_b}^{x} \left(\frac{A_0}{A(x')}\right)^{\frac{m}{n}} dx' \quad (6)$$

Where x_b is the base level, x is the distance from the base level upstream, A_0 is the reference drainage area (equal to 1), $\frac{m}{n}$ is the basin concavity (set to a standard value of 0.45) (Kirby and Whipple, 2012). In this equation, χ represents a position along a river or stream channel profile that results from integrating drainage area along a channel network from the base level (Perron and Royden, 2013; Willett et al., 2014; Gallen and Wegmann, 2017). When plotting χ vs. elevation of a river channel or tributary, the slope of the plot is the K_{sn} of the channel. χ is often used to analyze the past and present conditions of drainage basin boundaries and main channels (Perron and Royden, 2013; Willett et al., 2014).

To conduct a topographic analysis of the landscape, we acquired a 30-meter SRTM digital elevation model for the field area, distributed by OpenTopography.org (Rosen et al., 2000; Farr and Kobrick, 2000; Kobrick, 2006; Farr et al., 2007). We identified the outlet of the LCR northern contributing drainage basin (shown in Figure 1) and used it to delineate the basin and extract the DEM. The two main drainages in the study area, the WRV and MVW, and the third drainage, the Virgin River, all drain to the same pourpoint. We used the MATLAB package TopoToolbox to conduct the χ analysis and the published script, Chi Profiler (developed and demonstrated by Gallen and Wegmann, 2017), to delineate channel segments and analyze them in χ vs. elevation space (Schwanghart and Scherler, 2014; Gallen and Wegmann, 2017). We identified knickpoints by visual inspection of χ vs. elevation plots of delineated channel segments. K_{sn} was assessed above and below the knickpoint; knickpoints with K_{sn} differences of ≥ 20 were considered valid and recorded for plotting.

Cosmogenic data

Calculating a catchment-averaged erosion rate for the LCR drainage system allows us to understand the speed at which the landscape is changing and may have changed in the past.

Highly energized cosmic ray protons produced in outer space penetrate Earth's atmosphere and collide with atoms of atmospheric gases such as ^{16}O in a process known as spallation (Bierman et al., 2021). During the spallation of ^{16}O from the impact of a cosmic ray particle, meteoric ^{10}Be is produced, and protons and neutrons are released toward the Earth's surface (Bierman et al., 2021). As rock is exposed at Earth's surface, it is gradually bombarded with neutrons from atmospheric spallation. When a neutron makes contact with quartz (SiO_2) on Earth's surface, spallation occurs again, and ^{10}Be is produced and stored within the quartz crystal lattice (Bierman et al., 2021). ^{10}Be continues to accumulate in quartz the longer it is exposed at the surface. ^{10}Be has a half-life of 1.4 Ma and a production rate of 4-5 atoms/g per year (10^6 atoms/(cm^2*year) (Blanckenburg and Willenbring, 2014). Data derived from fluvial sediment collected from a basin reflects the average ^{10}Be concentration of fluvial sediments from all locations upstream of the sample collection point (Bierman et al., 2021), thus these catchment-averaged erosion rates are used to understand landscape erosion over large drainage areas. The catchment-wide ^{10}Be production rate $\overline{P}$ (g^{-1}/yr^{-1}) is calculated by:

$$\overline{P_i} = \frac{1}{S}\iint_S P_i(x,y) \cdot F_{topo} \cdot F_{glacier}(x,y) \cdot dx\, dy \qquad (7)$$

Where S is the basin area, $P_i(x,y)$ is the local production rate at a location in the catchment, and F_{topo} and $F_{glacier}$ are topographic shielding parameters (Lupker et al., 2012). The catchment averaged erosion rate $\overline{\varepsilon}$ (cm/yr^{-1}) is calculated by a rearranged equation (Brown et al., 1995; Lupker et al., 2012):

$$\overline{\varepsilon} = \frac{\left(\frac{\overline{P}_{ni}}{\mu n} + \frac{\overline{P}_{ms_i}}{\mu ms} + \frac{\overline{P}_{mf_i}}{\mu_f}\right)}{\overline{N}} \qquad (8)$$

where $\overline{P}_{ni}, \overline{P}_{ms_i}, \overline{P}_{mf_i}$ are the average catchment-wide ^{10}Be production rates (g^{-1}/yr^{-1}) resulting from the bombardment of quartz crystals by neutrons plus slow and fast muons. $\mu_i = (\rho/\Lambda_i)$ where ρ is the average density of the eroded material (quartz) (2.7g cm^{-3}) and Λ_i is the effective attenuation length of neutrons, slow muons, and fast muons $\left(\Lambda_n{\sim}160\ \Lambda_{\mu s}{\sim}\ 1500, \Lambda_{\mu f}{\sim}4300\ g\ cm^{-3}\right)$ (Braucher et al., 2011). $\overline{N}$ is the concentration of ^{10}Be atoms in a sediment sample (atoms/g^{-1}) (Brown et al., 1995; Lupker et al., 2012).

We collected four sediment samples from various locations along the Meadow Valley Wash (Figure 1). The sediment samples were processed at the Purdue Rare Isotope Measurement Laboratory (PRIME Lab) to measure concentrations of ^{10}Be (See appendix for sample processing details). We calculated catchment-averaged erosion rates as well as other catchment statistics from custom scripts that utilized equations 7 and 8 (Lupker et al., 2012; Gallen, 2021).

Knickpoint celerity model

We model the propagation and migration of a knickpoint initiating at 5.6 Ma at the outlet of the LCR northern catchment (Figures 1 and 3) to test whether it is physically plausible for a knickpoint initiating at 5.6 Ma to match our topographic observations. We use a knickpoint celerity model to simulate knickpoint propagation upstream as a response to base-level fall (Whittaker and Boulton, 2012). C_E represents the horizontal wave celerity of the kinematic wave, which is primarily controlled by the change in the contributing drainage area (*A*) along the drainage profile:

$$C_E \sim \Psi A^m S^{n-1} \quad (9)$$

where *S* is channel slope, *m* and *n* are erosional constants based on channel morphology, and Ψ is a variable that incorporates a range of geomorphic parameters including bedrock erodibility (Whipple and Tucker, 1999; Tucker and Whipple, 2002; Whipple, 2004; Whittaker et

al., 2008). The mathematical model we use, Knickretreat, is based on a modified version of equation 7 (Zondervan et al., 2020):

$$C_E = \mathrm{K}\Phi\sqrt{\mathrm{A}} \quad (10)$$

Here, Ψ from equation 7 is represented as $\mathrm{K}\Phi$, K is bedrock erodibility, Φ encompasses the scaling of discharge and channel width with downstream drainage area (Zondervan et al., 2020). This forward model is dependent on 1) two constant parameters: predicted age of the knickpoint (here, 5.6 Ma) and average annual precipitation (m yr^{-1}) and 2) four parameters extracted from points along a delineated drainage channel: downstream distance from the channel head, elevation, drainage area, and erosional efficiency (bedrock erodibility) ms^2kg^{-1}. The model output is a predicted knickpoint location (in the downstream distance) along the stream channel.

Zondervan et al. (2020) calculated K from equation 8 for catchments on the flanks of the Corinth Rift, Greece, using field-measured hydraulic parameters and calculated vertical incision rates from uplifted marine terraces and fluvial strath terraces. The main drainage channels in our field area have not been found to preserve datable abandoned surfaces to calculate K values for our field area. To address this issue, we used a grid search approach to systematically test erodibility value combinations for the different lithologies. We grouped lithologies in our study area into three units: Tertiary basin-fill sediments, Oligocene-to-Miocene caldera rim volcanics, and Cambrian-to-Triassic sedimentary rocks (Figure 3). To simplify our model, we classified lithologies along the main channel profile into two lithology groups: (1) Tertiary basin-fill and (2) Oligocene-to-Miocene caldera rim volcanics and Cambrian to Triassic sedimentary rocks (Figure 3b). We ran a range of erodibility values for each lithology through the Knickretreat model to calculate the predicted position of the knickpoint along the Meadow Valley Wash and

White River Valley. With the grid search, we tested every possible erosional efficiency value combination ranging from 1 x 10^{-11} to 1 x 10^{-13} ms^2kg^{-1} for both lithology 1 and lithology 2**,** where larger values indicate higher erosional efficiency. The grid search allows us to test if plausible erodibility parameters enable knickpoint migration up the catchment towards the known basin integration locations, and we can observe how changes in erodibility values for both lithology groups affect the knickpoint travel distance.

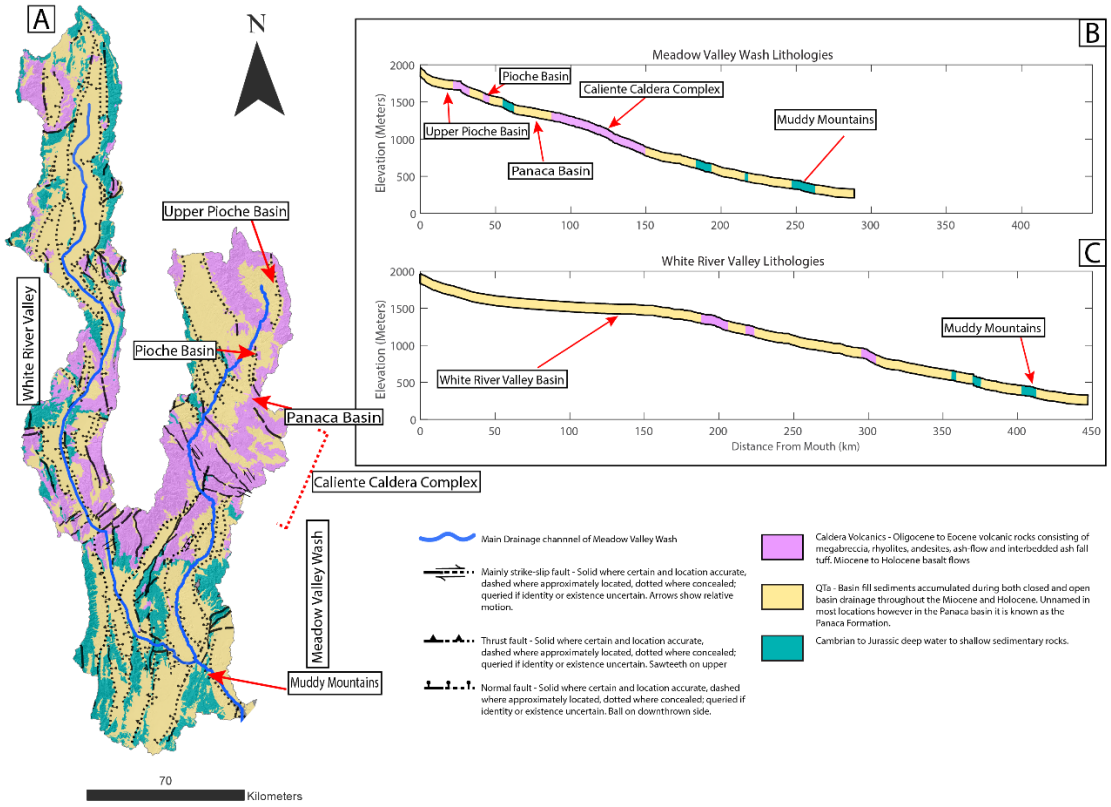

Figure 3. A) Simplified geologic map of the Meadow Valley Wash and White River Valley. B) Simplified surficial lithologies plotted along the channel profile of the Meadow Valley Wash. C) Simplified surficial lithologies plotted along the channel profile of the White River Valley.

RESULTS

Stream profile analysis and knickpoints

Our stream profile analysis began by evaluating the main channel profiles of the MVW, and WRV in distance vs. elevation and χ vs. elevation space. After ruling out steep segments caused by tectonic structures, lithologic boundaries, and confluences, we observed a knickpoint at ~800 m in the MVW and WRV (Figure 4). These knickpoints are characterized by the location of a change in K_{sn} from high to low in the upstream direction. K_{sn} is calculated by the slope of a segment along the χ vs elevation plot. We then looked at all second order channels joining the main trunk channel (125 in the MVW, 121 in the WRV, and 97 in the Virgin River). In the MVW, we identified 52 knickpoints characterized by a change in $K_{sn} \geq 20$ (Figure 4, Figure 5b, Figure 6b, Table 1). In the WRV, we identified 16 knickpoints (Figure 4, Figure 5a, Figure 6a, Table 2). In the Virgin River, we identified 50 knickpoints (Figure 4, Figure 5c, Figure 6c, Table 3).

Cosmogenic data

We collected four samples of modern sand along the main trunk channel of the MVW (locations in Figure 1). Catchment-averaged erosion rates calculated with sample location, contributing drainage area, channel steepness, and location-specific mean annual precipitation are listed in Table 3. There is a general trend of erosion rates decreasing with drainage area (Figure 7). The sediment samples yielded catchment-averaged erosion rates ranging from 19.6-54.8 mm/k.y. Sample MVW4 is from the lowest drainage area (farthest upstream) and yielded an erosion rate of 19.6 ± 4 mm/k.y. Going downstream, sample MVW6 yielded an erosion rate of 54.79 ± 4 mm/k.y. Sample MVW3 yielded an erosion rate of 44.69 ± 0.25 mm/k.y. Sample MVW2 yielded an erosion rate of 45.84 ± 0.044 mm/k.y.

Knickpoint celerity model

Our knickpoint celerity model incorporated an erodibility parameter grid search that tested erodibility values between 1 x 10^{-11} to 1 x 10^{-13} ms^2kg^{-1} for the two tested lithologies. The output of the model predicted knickpoint locations along the MVW and WRV after 5.6 Ma of simulated erosion. The Meadow Valley Wash model yielded predicted knickpoint locations between 6.5 and 279 km downstream from the channel head (Figure 8). The White River Valley model yielded predicted knickpoint locations between 37 and 437.5 km downstream of the channel head (Figure 8). The red equilibrium contour lines for each modeled drainage in Figure 8 show the specific erodibility parameter combinations that yield a predicted knickpoint location that matches the observed ~800-meter knickpoints in the MVW and WRV main channels.

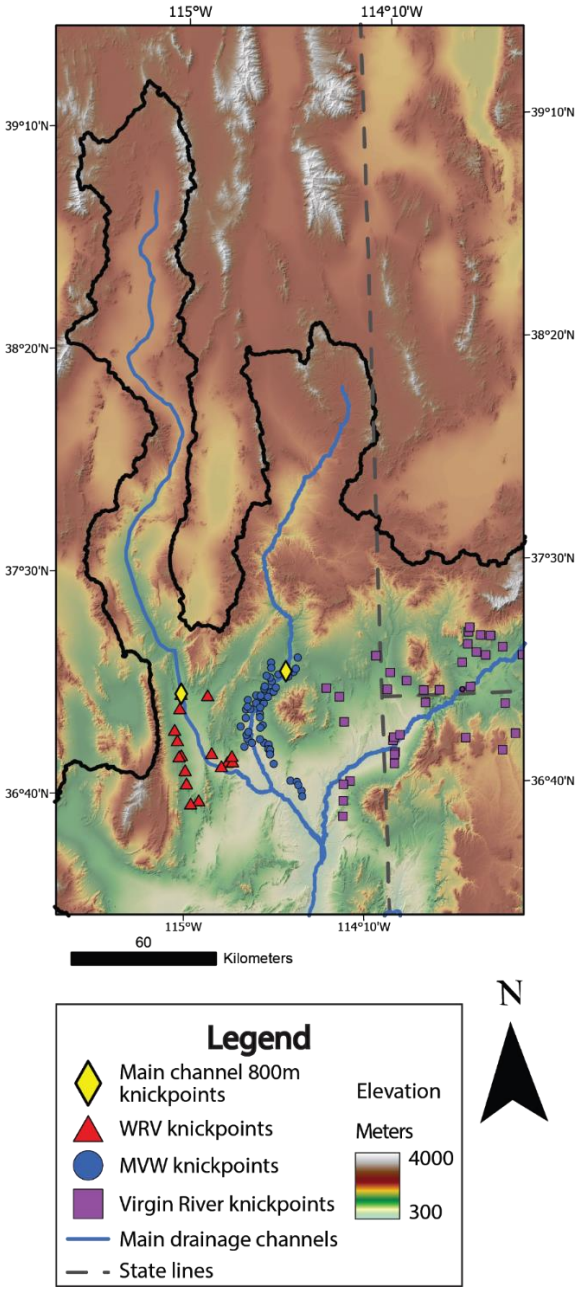

Figure 4. Map of study area depicting the spatial distribution of identified knickpoints in the studied drainages. Different knickpoint symbology used to differentiate catchment; WRV (red), MVW (blue), VR (purple).

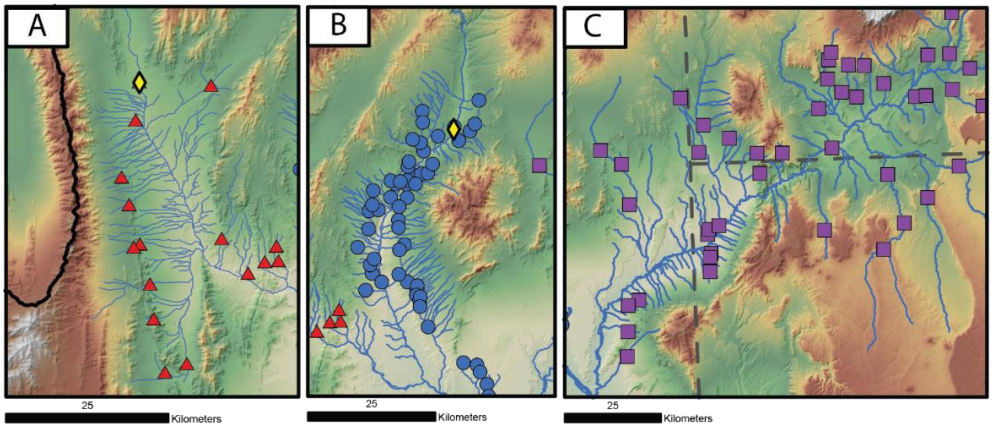

Figure 5. Inset map showing the identified knickpoints in A) White River Valley, B) Meadow Valley Wash, and C) Virgin River. Yellow diamond represents the ~800m main channel knickpoint. Different knickpoint symbology used to differentiate catchment; WRV (red), MVW (blue), VR (purple).

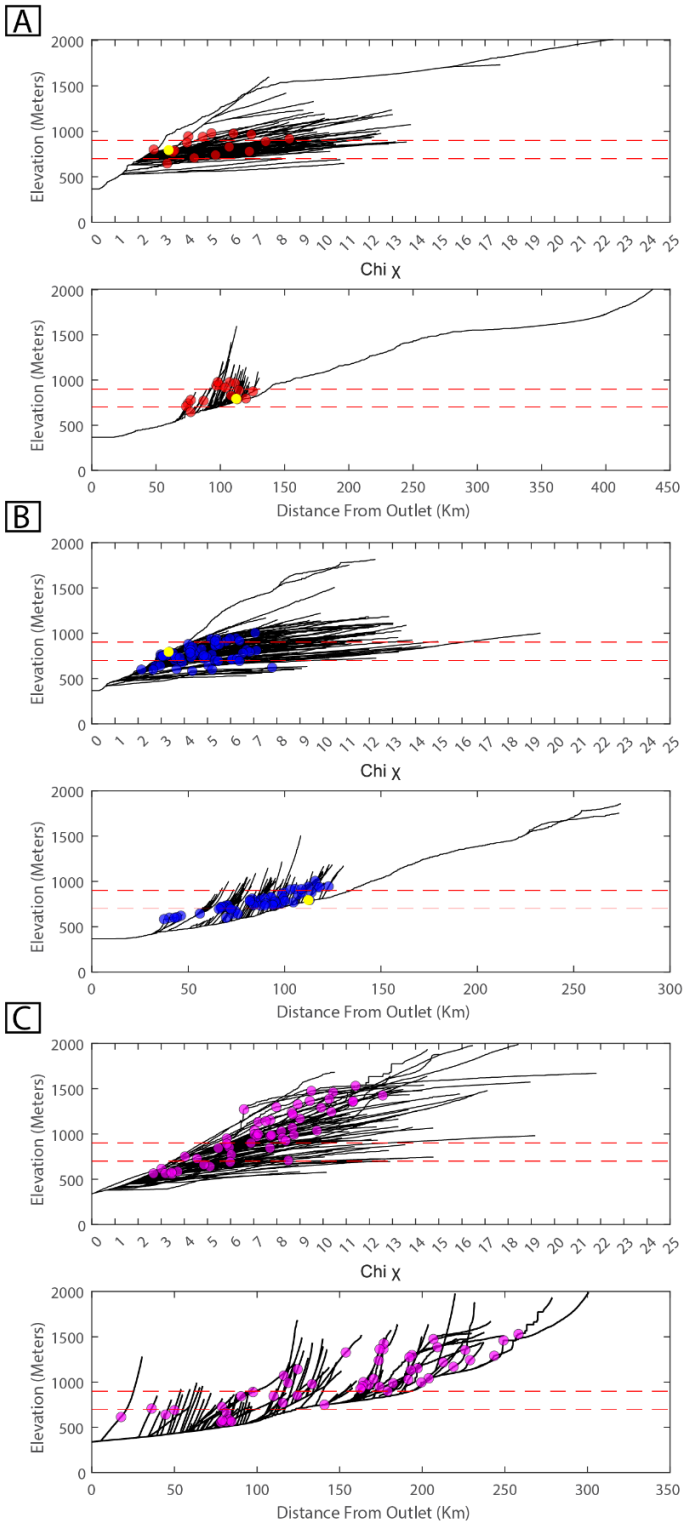

Figure 6. Knickpoints plotted on stream channels in units of distance vs. elevation and chi vs. elevation for the (A) White River Valley, (B) Meadow Valley Wash, and (C) Virgin River. The elevation band between 900 and 700 m (800 ± 100 m) is identified between the two horizontal dashed red lines on each plot. Yellow dots represent the ~800m main channel knickpoints in the MVW and WRV.

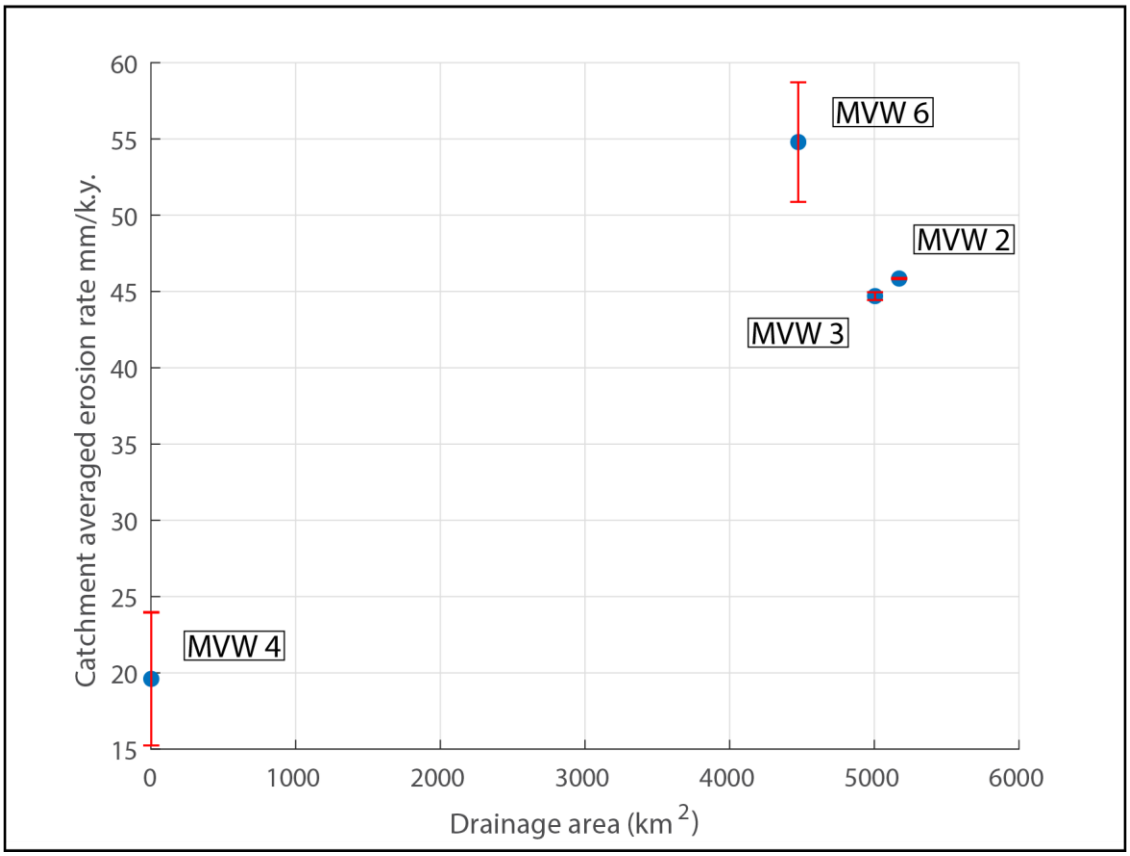

Figure 7. Erosion rate data for each sample plotted against contributing drainage area.

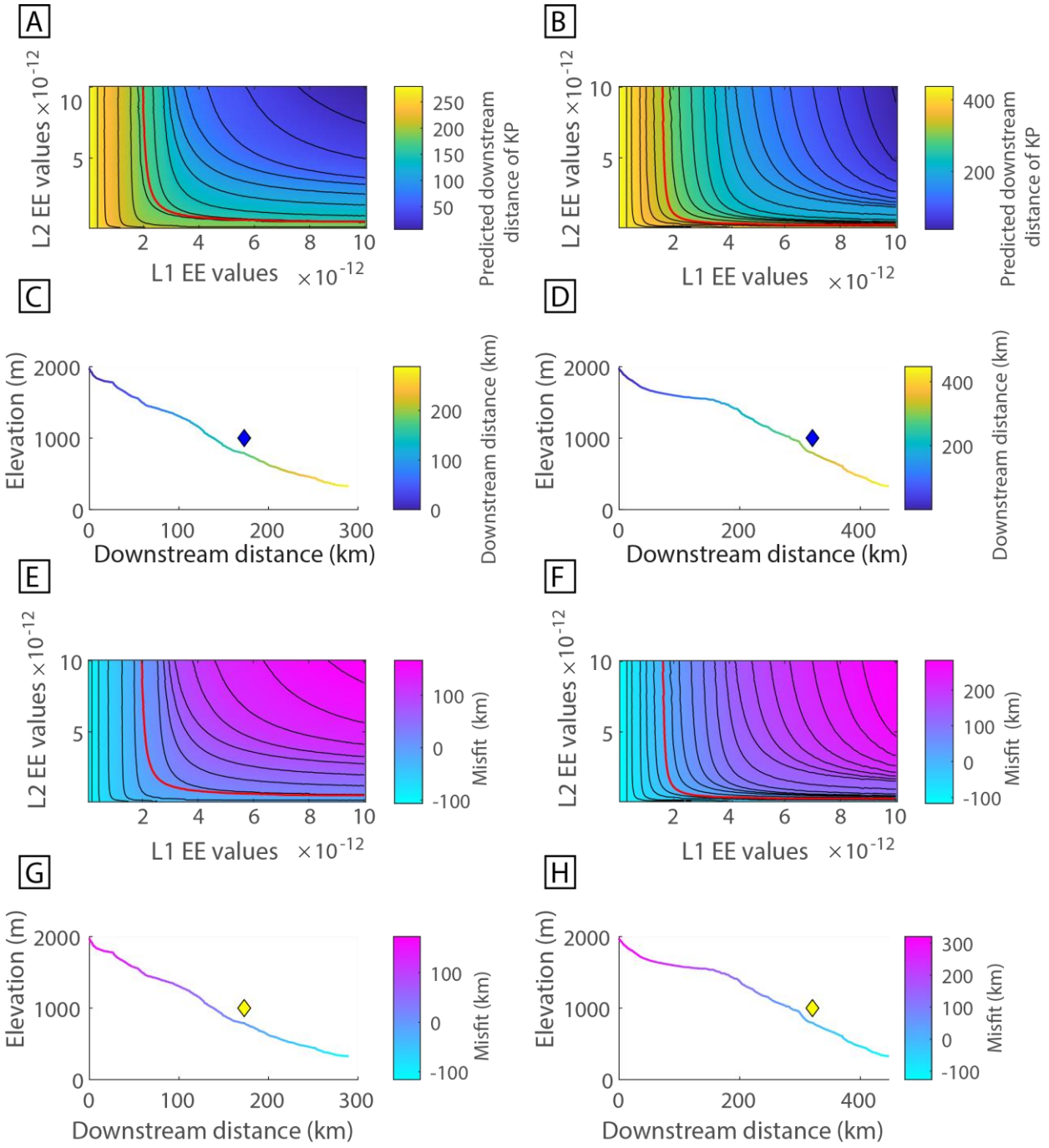

Figure 8. Knickpoint celerity model results for the Meadow Valley wash (A and C) and White River Valley (B and D) plotted as predicted downstream distance (yellow to blue) and as a misfit from the observed ~800m knickpoints (negative indicating predicted knickpoint was below the observed). The red equilibrium contour line represents the location of our initially interpreted ~800 m knickpoints within the parameter space for each tested drainage after 5.6 Ma of simulated erosion. E, F, G, and H represent results converted to a misfit from the observed 800 m knickpoint locations. Diamonds represent the location of the ~800m knickpoint along the channel profiles.

DISCUSSION

Knickpoint analysis: mapping and modeling

We test the possibility that the development of a through-going LCR in the Lake Mead area ca. 5.6 Ma would cause increased erosion, downcutting, and a lowering of the local catchment base level, generating knickpoint propagation into the study area catchments. Initial observations of the main channel profiles for the MVW and WRV indicate that they both have knickpoints at ~800 m asl. Assuming that erodibility (*K*) is constant throughout the catchment, knickpoints produced from a related base-level fall event (genetically related) should all plot at a similar χ distance, which includes knickpoints in the tributaries of the main channel (Perron and Royden, 2013). The two main channel knickpoints plotted in yellow in Figure 6a for the MVW and Figure 6b for the WRV lie at χ values of 3.34 and 2.68, being close in value but not equal. As seen in Figure 10, a few groups of mapped knickpoints lie at a similar χ distance; however, most of the mapped knickpoints are widely spread throughout χ space (Figure 10). These observations indicate there is not a significant population of knickpoints genetically related to the ~800 m knickpoints observed in the main channels.

We employed a knickpoint celerity model to evaluate knickpoint migration through the catchment over the last 5.6 m.y. This model, like all numerical models, has associated assumptions and limitations. Our knickpoint celerity model does not incorporate any topographic uplift and is influenced by erodibility (*K*) and drainage area. The model assumes that the contributing drainage area along the channel is fixed over time, making the amount of discharge constant throughout the 5.6 m.y. of modeled time. This model simulates physical erosion and does not factor in the chemical weathering of the stream channel. We assume erodibility to vary with lithology; larger erodibility values yield a higher erosional efficiency, and smaller

erodibility values yield a lower erosional efficiency. The goal of employing this model was not to isolate true erodibility parameters for the bedrock of the study area as done in Zondervan et al. (2020), but rather to test a range of potential erodibility parameters, investigating the possibility for a knickpoint to propagate far up the catchment and to the locations of the two ~800 m, main channel knickpoints in the MVW and WRV.

Our model shows that within our tested parameter space of erodibility values, a knickpoint can migrate up to and past the observed main channel knickpoints over 5.6 m.y. As seen in Figure 8 and mentioned above, our grid search model produced an equilibrium line of best-fit erodibility values for lithologies 1 and 2 that match our observed ~800 m main channel knickpoints. Model results show that input of a wide range of erodibility value combinations into the model fits our observed knickpoint locations. As lithology 1 erodibility values increase, erodibility values for Lithology 2 decrease to fit the observed. The same pattern is followed as lithology 2 values increase and lithology 1 values decrease to fit the observed knickpoint location. Zondervan et al. (2020) calculated erodibility values for their conglomerate and limestone lithologies of $1.8 \pm 0.3 \times 10^{-14}$ and $6 \pm 2 \times 10^{-15}$ ms^2kg^{-1} based on detailed field measurements of channel geometry and datable paleosurfaces. Our best-fit erodibility parameters for both the basin fill sediments (lithology 1) and Cambrian to Triassic sedimentary/Oligocene-to-Miocene caldera rim volcanic rocks (lithology 2) varied between 1×10^{-11} to 1×10^{-13} ms^2kg^{-1}, which are two orders of magnitudes larger than the erodibility values for the conglomerate lithology ($1.8 \pm 0.3 \times 10^{-14}$ ms^2kg^{-1}) and three orders of magnitude larger than the erodibility values for the limestone lithology ($6 \pm 2 \times 10^{-15}$ ms^2kg^{-1}) calculated by Zondervan et al. (2020) for the Corinth Rift, Greece. Zondervan et al. (2020) found that their erodibility values for limestones were similar to those in other studies when converting their erodibility values for their limestone lithology from

ms^2kg^{-1} (SI units) to m^{1-2m} yr^{-1}; however, for weaker lithologies, erodibility values from other studies span several orders of magnitude. Zondervan et al. (2020) conclude that it can be difficult to compare erodibility across different derivations of the stream power law and varying climate zones; therefore, we limit our comparison to Zondervan et al. (2020), who used the same parameterization and units.

The multi-order of magnitude differences in erodibility values between our studies and those discussed in Zondervan et al. (2020) suggest that for a knickpoint to migrate to our observed ~800 m location, erodibility values for the study area may have to be unreasonably high. Erodibility calculated from field measurements would be needed to more accurately model knickpoint migration in our field area and compare to other studies.

We conclude that while our model shows that it is possible for a knickpoint to migrate far up the MVW and WRV catchments, matching our observed main channel ~800 m knickpoints, the wide range of possible high erodibility value combinations for lithologies 1 and 2 indicate that we need a precise, field measured value of erodibility as done in Zondervan et al. (2020) to accurately model knickpoint migration in our study area. Therefore, at present given our current model's input parameters, we cannot confidently say that our knickpoint celerity model supports the genetic relationship of the ~800 m knickpoints in our field area.

Basin capture and changes in drainage area

Pleistocene basin capture events are interpreted to have occurred in both the WRV and MVW. The χ analysis and the knickpoint celerity model are based on the modern drainage basin because their calculations rely on a constant drainage area. When a basin capture event occurs the amount of contributing drainage area to a river system can increase drastically. The increase in drainage area following a capture will also increase the rates at which knickpoints migrate up

the main drainage channel as knickpoint migration depends on drainage area. This suggests that before the Pleistocene integration of endorheic basins in the MVW and WRV, knickpoint migration was slower than today based solely on contributing drainage areas. In a χ analysis, a river channel that has experienced basin integration will be shifted to a lower χ value, increasing its slope in a chi vs. elevation plot (Willett et al., 2014; Gallen and Wegmann, 2017). This suggests that if our main channel knickpoints were once coupled with genetically related knickpoints in the tributaries, its position in χ space could have been lowered and may have altered its correlation with other knickpoints in the χ vs. elevation plot. Modeling a basin capture in the Rhine River in Switzerland, Yanites et al. (2013) found that when a basin capture occurs, the rapid increase in drainage area creates a transient erosional response where a knickpoint is created that can propagate through the capturing and captured drainages. We suggest that the mechanism modeled by Yanites et al. (2013) may have also contributed to the decoupling of genetically related knickpoints and may have created additional knickpoints in the landscape not directly related to catchment base level fall.

Erosion rates

Our catchment-averaged erosion rates for the MVW are very low overall, ranging from 19.6 to 54 mm/k.y. This is most likely influenced by the extremely arid climate of southeast Nevada. Mean annual precipitation along the sample collection locations ranges from ~222 to 370 mm per year (Western Regional Climate Center). Researchers have often found a correlation between channel steepness and catchment averaged erosion rate (Kirby and Whipple, 2012; Harel et al., 2016). When comparing the MVW erosion rates to those of other arid regions around the world, we find that our samples have comparable catchment averaged erosion rates; however, the channel steepness of the MVW is notably higher compared to erosion rates of the

same magnitude (Figure 11). Compared to other erosion rates within the Basin and Range and Western U.S., our samples again show a much higher normalized channel steepness compared to catchments in the Wassuk Range in western Nevada (yellow) (Densmore et al., 2009) and east-central New Mexico (purple) (Bierman et al., 2005) (Figure 11). The high channel steepness values for relatively low catchment averaged erosion rates may also be explained by rapid incision following past basin capture. The slope of a river profile's χ vs. elevation plot is equal to the channel's k_{sn}. Willett et al. (2014) show that a basin capture can be identified in a river profile plotted in χ vs. elevation space where a steepened section in the profile occurs (high k_{sn}) and is accompanied by an incised canyon or gorge in the landscape. In the MVW, three basin captures connected by canyons are present. Spring Valley connects the highest elevated Upper-Pioche Basin to the Pioche Basin, Condor Canyon connects the Pioche Basin to the Panaca Basin, and Rainbow Canyon connects the Panaca Basin to the MVW (Figures 1 and 12). All three canyons exhibit increased k_{sn} values as seen in Figure 12. Sample MVW 2 was taken just below Rainbow Canyon, and samples MVW 3 and MVW 6 were taken within Rainbow Canyon; therefore, we suggest that the past basin integrations combined with the arid modern climate are the reasons behind the high channel steepness with relatively low catchment averaged erosion rates.

Climate

Precipitation directly contributes to discharge in river systems. Today, the climate of the Basin and Range is extremely arid. Within our study area in southeastern Nevada modern mean annual precipitation ranges from ~222 to 370 mm. However, research has shown that late-Pliocene through Pleistocene climatic conditions throughout the Basin and Range were wetter than modern, creating pluvial lake systems within the Great Basin (Ibarra et al., 2018; Abell et

al., 2021). Higher levels of precipitation would have a profound effect on erosion rates making them variable over the past 5.6 Ma, as erodibility (k) in the stream power incision law (equation 1) incorporates climatic factors. Our knickpoint celerity model utilizes a modern mean annual precipitation set to 258 mm per year. While only active flow occurs from stochastic precipitation events, we assume over million-year time scales flow is more active. We suggest that wetter conditions, sufficient to fill lakes in endorheic basins, would drastically increase the distance and speed of propagation of a knickpoint generated 5.6 Ma compared to what we found in our model. If true erodibility values are lower than what we modeled as discussed above, the higher Plio-Pleistocene precipitation may have accounted for lower bedrock erodibility allowing for further and faster knickpoint propagation.

Regional Context

The Virgin River, while not the focus of our study, is part of the LCR northern catchment. In a geochronology and provenance study, Walk et al. (2019) investigated the age and arrival of the Virgin River to the LCR catchment. They found that the Virgin River once existed as a closed, endorheic basin and became integrated into the LCR ca. 5 Ma. Since then, the Virgin River has produced an additional 1 km of incision due to mantle-driven geodynamic uplift. We posit that the Colorado Plateau geodynamic uplift may have contributed to the overall high channel steepness found within the MVW, as it exists at the boundary between the Basin and Range and Colorado Plateau, and the impacts from dynamic topography are experienced over wavelengths of hundreds to thousands of kilometers (Braun, 2010).

A tuff geochemically correlated to the Upper Horse Hill Ash within the Upper Muddy Creek Formation of the Glendale basin (Figure 1), leads to the interpretation that the Glendale basin did not become incorporated into the externally drained catchment of the LCR until after 3

Ma (Pederson, 1999; Pederson et al., 2001; Dickinson et al., 2014; Walk et al., 2019). The age constraint of the Upper Horse Hill Ash was not conducted with precise radiometric dating but with an age/depth curve estimation (Williams, 1994). We suggest an accurate age date be made to support the interpretation that the MVW and lower WRV became integrated into the LCR catchment after 3 Ma. If the integration had occurred after 3 Ma, our hypothesis of knickpoint propagation starting at 5.6 Ma may have been slower than modeled, contributing to the integration of the Glendale Basin through the Muddy Mountains ca 3 Ma.

Integration History

There are three hypotheses for drainage basin integration in the Basin and Range: 1) a top-down mechanism where basins fill with water and sediment, eventually spilling over the drainage divide (i.e. the basin spillover hypothesis), 2) a bottom-up basin capture mechanism whereby channel-head erosion from an adjacent basin erodes through the drainage divide and captures a neighboring basin, and 3) a combination of mechanisms 1 and 2 (Pederson, 2008; Meek, 2019; Hilgendorf et al., 2020; Larson et al., 2022). While Meek, (2019) argues for the top-down integration mechanism along the MVW, the landscape of southeastern Nevada is complex. Factoring in climatic and multiple geologic variables, including lithology variation, large-scale structures, and geodynamics over the past 5.6 m.y., makes the model extremely complicated. We suggest that the mechanisms that formed the modern catchment of the LCR, specifically the MVW and WRV, resulted from a complex interplay of contributing factors that we have discussed above supporting the interpretation from Pederson, (2008). Wet Plio-Pleistocene climatic conditions combined with knickpoint propagation caused by increased stream power and downcutting of the Lake Mead area, lead to increased channel head erosion from the LCR

side of the catchment. Concurrently, the increased precipitation likely contributed to the overfilling of the Panaca, Pioche, and Upper Pioche basins, with the formation of pluvial lakes initiating basin spillover mechanics to connect the channel head erosion from the LCR.

Future work

While we have made progress regarding the drainage divide history between the LCR and Great Basin catchments in Southeastern Nevada, future work is still needed regarding the timing and mechanisms of basin integration. Detailed tephrostratigraphic surveys in previously endorheic basins along the MVW and WRV that incorporate radiometric dates of the highest elevated tephra within basin fill deposits may allow for detailed timing constraints on basin integration history as only relative estimations for the integration of the Panaca basin, WRV upper basin, and the Glendale basin have been made. Landscape evolution modeling that can account for multiple variables, including accurate variations in bedrock erodibility and changes in precipitation and drainage area over time, coupled with basin integration timing constraints, could result in a well-tuned model for the drainage basin evolution history of Southeastern Nevada.

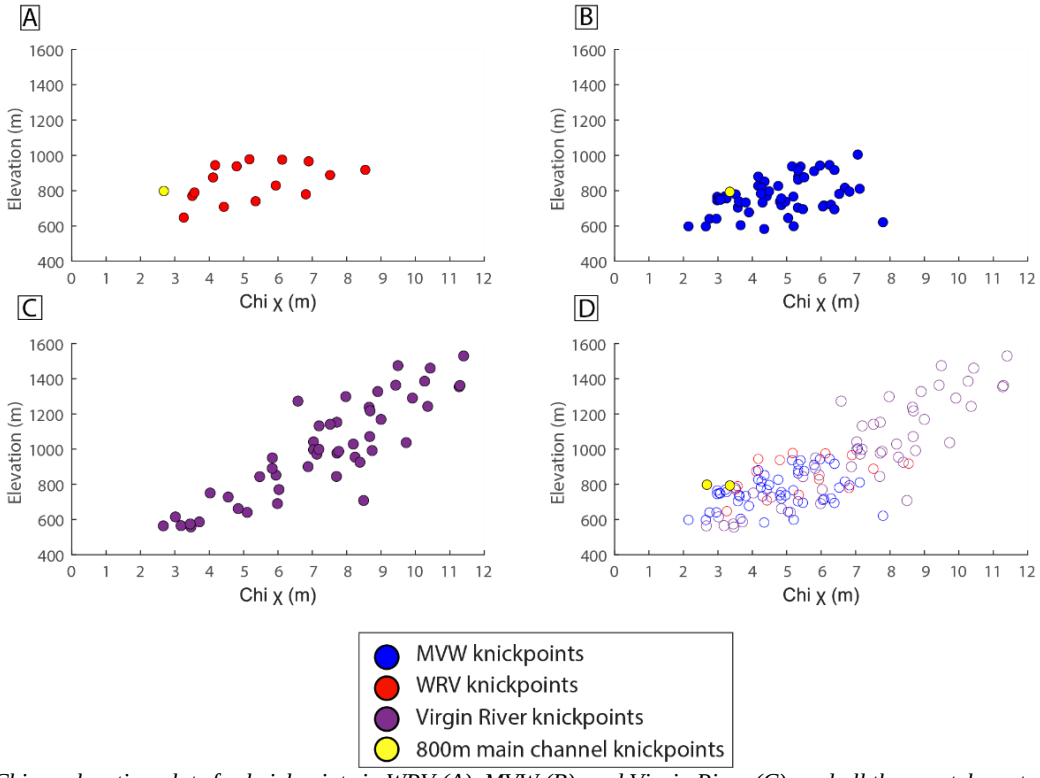

Figure 9. Chi vs. elevation plots for knickpoints in WRV (A), MVW (B), and Virgin River (C), and all three catchments (D).

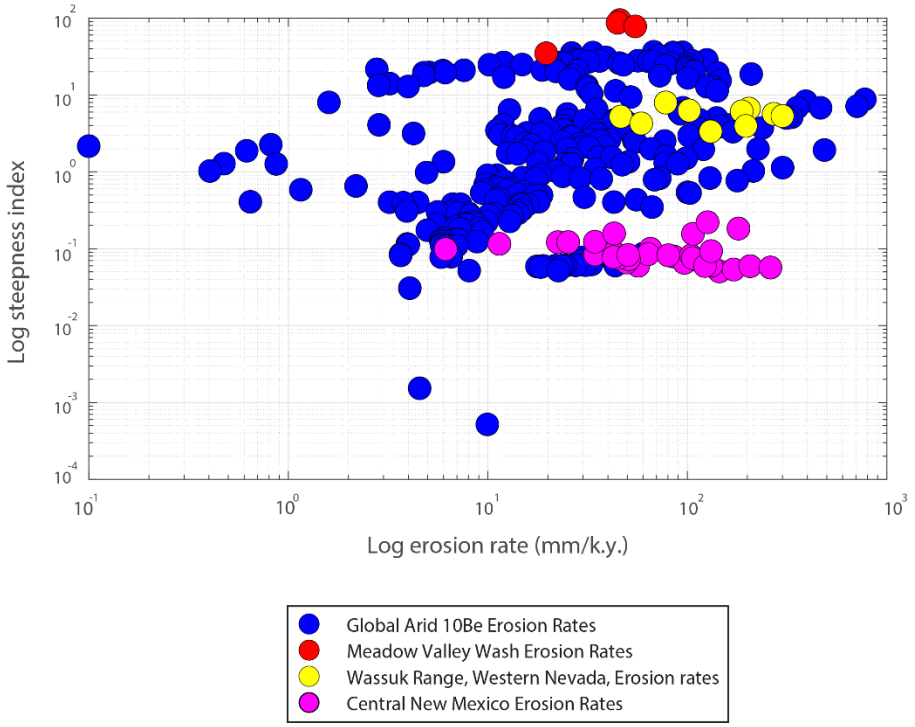

Figure 10. Globally compiled catchment averaged erosion rates plotted against channel steepness compiled by Harel et al.(2016). The red data points are samples collected from the MVW. The yellow data points are from the western Nevada Basin and Range, and the purple data points are from east-central New Mexico.

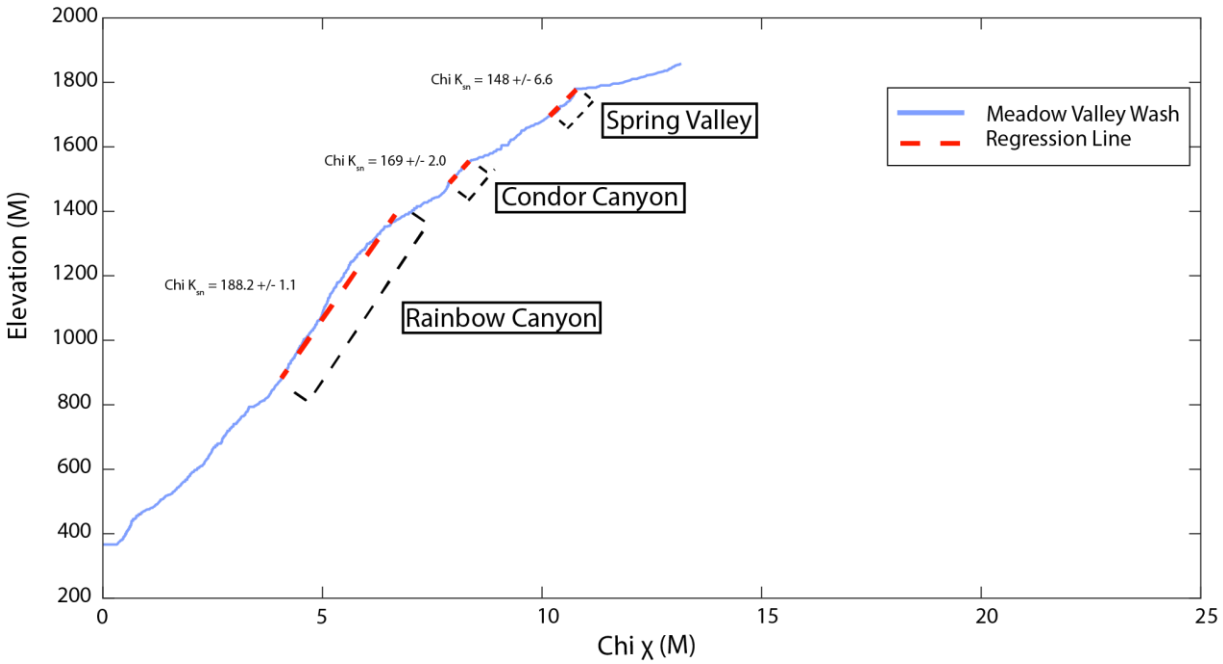

Figure 11. Profiles of the MVW are plotted in chi vs. elevation space. Ksn of incised canyons along the MVW plotted.

Conclusion

This study took a multifaceted approach to investigate the erosion history of the Meadow Valley Wash (MVW) and White River Valley (WRV), focusing on topographic knickpoint analysis, knickpoint modeling, and cosmogenic erosion rates. While initial ~800m knickpoints in the main channels of the MVW and WRV seemed to be related, a chi analysis of the tributaries indicated that tributary knickpoints do not show a genetic relation to the main channel knickpoints. If knickpoints were once related, the decoupling of genetically related knickpoints may be due to the rapid increase in drainage area from basin integration events over the past 5.6 Ma.

The knickpoint celerity model indicates that a knickpoint can propagate far up the MVW and WRV, potentially reaching the location of the ~800 m knickpoints over 5.6 m.y. However, our erodibility values used in the model are higher than those used in other regions, suggesting that further field-calibrated erodibility parameters are necessary for more accurate modeling.

The MVW's modern catchment is eroding between 19.6 and 54.8 mm per k.y., which is comparable to other arid regions; however, it is slow for the catchment’s normalized channel steepness. This discrepancy is most likely caused by southeastern Nevada's extremely arid modern climate and basin integration events that created the rapidly incised, steep canyons along the MVW.

We suggest future work on this problem should take two approaches. 1) a focus on tephrostratigraphic work within formerly endorheic basins to more precisely constrain the timing of basin integration. 2) landscape evolution models that can account for lithologically variable bedrock erodibility, past precipitation changes, and basin integrations will further develop the

model of landscape evolution in southeastern Nevada and the drainage divide history between the catchment of the lower Colorado River and Great Basin.

Our evidence supports mechanism three as the likely driving force behind the development of the LCR's modern catchment. A combination of basin spill-over from endorheic basins and higher-than-modern channel head erosion from the LCR side of the drainage divide formed the modern catchment.

REFERENCES

Abell, J.T., Winckler, G., Anderson, R.F., and Herbert, T.D., 2021, Poleward and weakened westerlies during Pliocene warmth: Nature, v. 589, p. 70–75, doi:10.1038/s41586-020-03062-1.

Armstrong, R.L., 1968, Sevier Orogenic Belt in Nevada and Utah: Geological Society of America Bulletin, v. 79, p. 429, doi:10.1130/0016-7606(1968)79[429:SOBINA]2.0.CO;2.

Best, M.G., Christiansen, E.H., and Blank, Jr., R.H., 1989, Oligocene caldera complex and calc-alkaline tuffs and lavas of the Indian Peak volcanic field, Nevada and Utah: Geological Society of America Bulletin, v. 101, p. 1076–1090, doi:10.1130/0016-7606(1989)101<1076:OCCACA>2.3.CO;2.

Best, M.G., Christiansen, E.H., De Silva, S., and Lipman, P.W., 2016, Slab-rollback ignimbrite flareups in the southern Great Basin and other Cenozoic American arcs: A distinct style of arc volcanism: Geosphere, v. 12, p. 1097–1135, doi:10.1130/GES01285.1.

Best, M.G., Christiansen, E.H., and Gromme, S., 2013a, Introduction: The 36-18 Ma southern Great Basin, USA, ignimbrite province and flareup: Swarms of subduction-related supervolcanoes: Geosphere, v. 9, p. 260–274, doi:10.1130/GES00870.1.

Best, M.G., Gromme, Sherman., Deino, A.L., Christiansen, E.H., Hart, G.L., and Tingey, D.G., 2013b, The 36–18 Ma Central Nevada ignimbrite field and calderas, Great Basin, USA: Multicyclic super-eruptions: Geosphere, v. 9, p. 1562–1636, doi:10.1130/GES00945.1.

Bidgoli, T.S., Stockli, D.F., and Walker, J.D., 2015, Low-temperature thermochronologic constraints on the kinematic histories of the Castle Cliffs, Tule Springs, and Mormon Peak detachments, southwestern Utah and southeastern Nevada: Geosphere, v. 11, p. 850–867, doi:10.1130/GES01083.1.

Bierman, P.R., Bender, A.M., Christ, A.J., Corbett, L.B., Halsted, C.T., Portenga, E.W., and Schmidt, A.H., 2021, Dating by Cosmogenic Nuclides, *in* Alderton, D. and Elias, S.A. eds., Encyclopedia of Geology (Second Edition), Oxford, Academic Press, p. 101–115, doi:10.1016/B978-0-08-102908-4.00124-7.

Bierman, P.R., Reuter, J.M., Pavich, M., Gellis, A.C., Caffee, M.W., and Larsen, J., 2005, Using cosmogenic nuclides to contrast rates of erosion and sediment yield in a semi-arid, arroyo-dominated landscape, Rio Puerco Basin, New Mexico: Earth Surface Processes and Landforms, v. 30, p. 935–953, doi:10.1002/esp.1255.

Blanckenburg, F. von, and Willenbring, J.K., 2014, Cosmogenic Nuclides: Dates and Rates of Earth-Surface Change: Elements, v. 10, p. 341–346, doi:10.2113/gselements.10.5.341.

Braucher, R., Merchel, S., Borgomano, J., and Bourlès, D.L., 2011, Production of cosmogenic radionuclides at great depth: A multi element approach: Earth and Planetary Science Letters, v. 309, p. 1–9, doi:10.1016/j.epsl.2011.06.036.

Braun, J., 2010, The many surface expressions of mantle dynamics: Nature Geoscience, v. 3, p. 825–833, doi:10.1038/ngeo1020.

Brown, E.T., Stallard, R.F., Larsen, M.C., Raisbeck, G.M., and Yiou, F., 1995, Denudation rates determined from the accumulation of in situ-produced 10Be in the luquillo experimental forest, Puerto Rico: Earth and Planetary Science Letters, v. 129, p. 193–202, doi:10.1016/0012-821X(94)00249-X.

Crow, R.S., Schwing, J., Karlstrom, K.E., Heizler, M., Pearthree, P.A., House, P.K., Dulin, S., Jänecke, S.U., Stelten, M., and Crossey, L.J., 2021, Redefining the age of the lower Colorado River, southwestern United States: Geology, v. 49, p. 635–640, doi:10.1130/G48080.1.

DeCelles, P.G., 2004, Late Jurassic to Eocene evolution of the Cordilleran thrust belt and foreland basin system, western U.S.A.: American Journal of Science, v. 304, p. 105–168, doi:10.2475/ajs.304.2.105.

Densmore, A.L., Hetzel, R., Ivy-Ochs, S., Krugh, W.C., Dawers, N., and Kubik, P., 2009, Spatial variations in catchment-averaged denudation rates from normal fault footwalls: Geology, v. 37, p. 1139–1142, doi:10.1130/G30164A.1.

Dickinson, W.R., Karlstrom, K.E., Hanson, A.D., Gehrels, G.E., Pecha, M., Cather, S.M., and Kimbrough, D.L., 2014, Detrital-zircon U-Pb evidence precludes paleo–Colorado River sediment in the exposed Muddy Creek Formation of the Virgin River depression: Geosphere, v. 10, p. 1123–1138, doi:10.1130/GES01097.1.

Diguiseppi, W.H., and Bartley, J.M., 1991, Stratigraphic effects of change from internal to external drainage in an extending basin, southeastern Nevada: Geological Society of America Bulletin, v. 103, p. 48–55, doi:10.1130/0016-7606(1991)103<0048:SEOCFI>2.3.CO;2.

Farr, T.G. et al., 2007, The Shuttle Radar Topography Mission: Reviews of Geophysics, v. 45, p. 2005RG000183, doi:10.1029/2005RG000183.

Farr, T.G., and Kobrick, M., 2000, Shuttle radar topography mission produces a wealth of data: Eos, Transactions American Geophysical Union, v. 81, p. 583–585, doi:10.1029/EO081i048p00583.

Faulds, J.E., Schreiber, B.C., Langenheim, V.E., Hinz, N.H., Shaw, T.H., Heizler, M.T., Perkins, M.E., El Tabakh, M., and Kunk, M.J., 2016, Paleogeographic implications of late Miocene lacustrine and nonmarine evaporite deposits in the Lake Mead region: Immediate precursors to the Colorado River: Geosphere, v. 12, p. 721–767, doi:10.1130/GES01143.1.

Flint, J.J., 1974, Stream gradient as a function of order, magnitude, and discharge: Water Resources Research, v. 10, p. 969–973, doi:10.1029/WR010i005p00969.

Gallen, S.F., 2021, sfgallen/sfg_topotoolbox_addons:, https://github.com/sfgallen/sfg_topotoolbox_addons (accessed May 2024).

Gallen, S.F., and Wegmann, K.W., 2017, River profile response to normal fault growth and linkage: an example from the Hellenic forearc of south-central Crete, Greece: Earth Surface Dynamics, v. 5, p. 161–186, doi:10.5194/esurf-5-161-2017.

Gallen, S.F., Wegmann, K.W., and Bohnenstieh, D.R., 2013, Miocene rejuvenation of topographic relief in the southern Appalachians: GSA Today, v. 23, p. 4–10, doi:10.1130/GSATG163A.1.

Harel, M.-A., Mudd, S.M., and Attal, M., 2016, Global analysis of the stream power law parameters based on worldwide 10Be denudation rates: Geomorphology, v. 268, p. 184–196, doi:10.1016/j.geomorph.2016.05.035.

Harkins, N., Kirby, E., Heimsath, A., Robinson, R., and Reiser, U., 2007, Transient fluvial incision in the headwaters of the Yellow River, northeastern Tibet, China: Journal of Geophysical Research: Earth Surface, v. 112, doi:10.1029/2006JF000570.

Hilgendorf, Z., Wells, G., Larson, P.H., Millett, J., and Kohout, M., 2020, From basins to rivers: Understanding the revitalization and significance of top-down drainage integration mechanisms in drainage basin evolution: Geomorphology, v. 352, p. 107020, doi:10.1016/j.geomorph.2019.107020.

Howard, A.D., 1994, A detachment-limited model of drainage basin evolution: Water Resources Research, v. 30, p. 2261–2285, doi:10.1029/94WR00757.

Ibarra, D.E., Oster, J.L., Winnick, M.J., Rugenstein, J.K.C., Byrne, M.P., and Chamberlain, C.P., 2018, Warm and cold wet states in the western United States during the Pliocene–Pleistocene: Geology, v. 46, p. 355–358, doi:10.1130/G39962.1.

Kirby, E., and Whipple, K.X., 2012, Expression of active tectonics in erosional landscapes: Journal of Structural Geology, v. 44, p. 54–75, doi:10.1016/j.jsg.2012.07.009.

Kobrick, M., 2006, On the Toes of Giants - How SRTM was Born: Photogrammetric Engineering and Remote Sensing, https://www.semanticscholar.org/paper/On-the-Toes-of-Giants-How-SRTM-was-Born-Kobrick/bcae45486e6992249bd1862321d3bf444fa6b5a7 (accessed May 2024).

Larson, P.H., Dorn, R.I., Gootee, B.F., and Seong, Y.B., 2022, Drainage integration in extensional tectonic settings: Geomorphology, v. 399, p. 108082, doi:10.1016/j.geomorph.2021.108082.

Liberty, L.M., Heller, P.L., and Smithson, S.B., 1994, Seismic reflection evidence for two-phase development of Tertiary basins from east-central Nevada: Geological Society of America Bulletin, v. 106, p. 1621–1633, doi:10.1130/0016-7606(1994)106<1621:SREFTP>2.3.CO;2.

Lupker, M., Blard, P.-H., Lavé, J., France-Lanord, C., Leanni, L., Puchol, N., Charreau, J., and Bourlès, D., 2012, 10Be-derived Himalayan denudation rates and sediment budgets in the Ganga basin: Earth and Planetary Science Letters, v. 333–334, p. 146–156, doi:10.1016/j.epsl.2012.04.020.

Meek, N., 2019, Episodic forward prolongation of trunk channels in the Western United States: Geomorphology, v. 340, p. 172–183, doi:10.1016/j.geomorph.2019.05.002.

Merritts, D., and Vincent, K.R., 1989, Geomorphic response of coastal streams to low, intermediate, and high rates of uplift, Medocino triple junction region, northern California: Geological Society of America Bulletin, v. 101, p. 1373–1388, doi:10.1130/0016-7606(1989)101<1373:GROCST>2.3.CO;2.

Miller, E.L., Dumitru, T.A., Brown, R.W., and Gans, P.B., 1999, Rapid Miocene slip on the Snake Range-Deep Creek Range fault system, east-central Nevada: Geological Society of America Bulletin, v. 111, p. 886–905, doi:10.1130/0016-7606(1999)111<0886:RMSOTS>2.3.CO;2.

Pazzaglia, F.J., Gardner, T.W., and Merritts, D.J., 1998, Bedrock fluvial incision and longitudinal profile development over geologic time scales determined by fluvial terraces, *in* Tinkler, J. and Wohl, E. eds., Geophysical Monograph Series, Washington, D. C., American Geophysical Union, v. 107, p. 207–235, doi:10.1029/GM107p0207.

Pederson, J.L., 1999, A long-term record of climate-controlled hillslope sedimentation [Dissertation]: University of New Mexico, 235 p.

Pederson, J.L., 2008, The mystery of the pre–Grand Canyon Colorado River—Results from the Muddy Creek Formation: GSA Today, v. 18, p. 4, doi:10.1130/GSAT01803A.1.

Pederson, J.L., Pazzaglia, F.J., Smith, G.A., and Mou, Y., 2000, Neogene through Quaternary hillslope records, basin sedimentation, and landscape evolution of southeastern Nevada, *in* GSA Field Guide 2: Great Basin and Sierra Nevada, Geological Society of America, v. 2, p. 117–134, doi:10.1130/0-8137-0002-7.117.

Pederson, J., Smith, G., and Pazzaglia, F., 2001, Comparing the modern, Quaternary, and Neogene records of climate-controlled hillslope sedimentation in southeast Nevada: Geological Society of America Bulletin, v. 113, p. 305–319, doi:10.1130/0016-7606(2001)113<0305:CTMQAN>2.0.CO;2.

Perron, J.T., and Royden, L., 2013, An integral approach to bedrock river profile analysis: Earth Surface Processes and Landforms, v. 38, p. 570–576, doi:10.1002/esp.3302.

Phoenix, D.A., 1948, Geology and ground water on the Meadow Valley Wash drainage area, Nevada, above the vicinity of Caliente, Nevada: Office of State Engineer Water Resources Bulletin 7:1-117.

Purdue Rare Isotope Measurement Laboratory Mineral Separation Procedure: Purdue Rare Isotope Measurement Laboratory: Purdue University:,

https://www.physics.purdue.edu/primelab/labs/mineral-separation-lab/procedure.php (accessed June 2024).

Rosen, P.A., Hensley, S., Joughin, I.R., Li, F.K., Madsen, S.N., Rodriguez, E., and Goldstein, R.M., 2000, Synthetic aperture radar interferometry: Proceedings of the IEEE, v. 88, p. 333–382, doi:10.1109/5.838084.

Roskowski, J.A., Patchett, P.J., Spencer, J.E., Pearthree, P.A., Dettman, D.L., Faulds, J.E., and Reynolds, A.C., 2010, A late Miocene-early Pliocene chain of lakes fed by the Colorado River: Evidence from Sr, C, and O isotopes of the Bouse Formation and related units between Grand Canyon and the Gulf of California: Geological Society of America Bulletin, v. 122, p. 1625–1636, doi:10.1130/B30186.1.

Rowley, P.D. et al., 2017, Geology and geophysics of White Pine and Lincoln counties, Nevada, and adjacent parts of Nevada and Utah: the geologic framework of regional groundwater flow systems [TEXT AND 4 PLATES]:, https://pubs.nbmg.unr.edu/product-p/r056.htm (accessed May 2024).

Rowley, P.D., Steven, T.A., and Mehnert, H.H., 1981, Origin and structural implications of upper Miocene rhyolites in Kingston Canyon, Piute County, Utah: Geological Society of America Bulletin, v. 92, p. 590, doi:10.1130/0016-7606(1981)92<590:OASIOU>2.0.CO;2.

Schwanghart, W., and Scherler, D., 2014, Short Communication: TopoToolbox 2 – MATLAB-based software for topographic analysis and modeling in Earth surface sciences: Earth Surface Dynamics, v. 2, p. 1–7, doi:10.5194/esurf-2-1-2014.

Snyder, N.P., Whipple, K.X., Tucker, G.E., and Merritts, D.J., 2000, Landscape response to tectonic forcing: Digital elevation model analysis of stream profiles in the Mendocino triple junction region, northern California: GSA Bulletin, v. 112, p. 1250–1263, doi:10.1130/0016-7606(2000)112<1250:LRTTFD>2.0.CO;2.

Spencer, J.E., Patchett, P.J., Pearthree, P.A., House, P.K., Sarna-Wojcicki, A.M., Wan, E., Roskowski, J.A., and Faulds, J.E., 2013, Review and analysis of the age and origin of the Pliocene Bouse Formation, lower Colorado River Valley, southwestern USA: Geosphere, v. 9, p. 444–459, doi:10.1130/GES00896.1.

Tucker, G.E., and Whipple, K.X., 2002, Topographic outcomes predicted by stream erosion models: Sensitivity analysis and intermodel comparison: Journal of Geophysical Research: Solid Earth, v. 107, doi:10.1029/2001JB000162.

Walk, C.J., Karlstrom, K.E., Crow, R.S., and Heizler, M.T., 2019, Birth and evolution of the Virgin River fluvial system: ~1 km of post–5 Ma uplift of the western Colorado Plateau: Geosphere, v. 15, p. 759–782, doi:10.1130/GES02019.1.

Western Regional Climate Center Nevada Climate Data:, https://wrcc.dri.edu/summary/Climsmnv.html (accessed June 2024).

Whipple, K.X., 2004, BEDROCK RIVERS AND THE GEOMORPHOLOGY OF ACTIVE OROGENS: Annual Review of Earth and Planetary Sciences, v. 32, p. 151–185, doi:10.1146/annurev.earth.32.101802.120356.

Whipple, K.X., and Tucker, G.E., 1999, Dynamics of the stream-power river incision model: Implications for height limits of mountain ranges, landscape response timescales, and research needs: Journal of Geophysical Research: Solid Earth, v. 104, p. 17661–17674, doi:10.1029/1999JB900120.

Whittaker, A.C., Attal, M., Cowie, P.A., Tucker, G.E., and Roberts, G., 2008, Decoding temporal and spatial patterns of fault uplift using transient river long profiles: Geomorphology, v. 100, p. 506–526, doi:10.1016/j.geomorph.2008.01.018.

Whittaker, A.C., and Boulton, S.J., 2012, Tectonic and climatic controls on knickpoint retreat rates and landscape response times: Journal of Geophysical Research: Earth Surface, v. 117, doi:10.1029/2011JF002157.

Willett, S.D., McCoy, S.W., Perron, J.T., Goren, L., and Chen, C.-Y., 2014, Dynamic Reorganization of River Basins: Science, v. 343, p. 1248765, doi:10.1126/science.1248765.

Williams, S.K., 1994, Late Cenozoic tephrostratigraphy of deep sediment cores from the Bonneville Basin, northwest Utah: Geological Society of America Bulletin, v. 106, p. 1517–1530, doi:10.1130/0016-7606(1994)105<1517:LCTODS>2.3.CO;2.

Wobus, C., Whipple, K.X., Kirby, E., Snyder, N., Johnson, J., Spyropolou, K., Crosby, B., and Sheehan, D., 2006, Tectonics from topography: Procedures, promise, and pitfalls:, doi:10.1130/2006.2398(04).

Yanites, B.J., Ehlers, T.A., Becker, J.K., Schnellmann, M., and Heuberger, S., 2013, High magnitude and rapid incision from river capture: Rhine River, Switzerland: Journal of Geophysical Research: Earth Surface, v. 118, p. 1060–1084, doi:10.1002/jgrf.20056.

Yonkee, W.A., and Weil, A.B., 2015, Tectonic evolution of the Sevier and Laramide belts within the North American Cordillera orogenic system: Earth-Science Reviews, v. 150, p. 531–593, doi:10.1016/j.earscirev.2015.08.001.

Zondervan, J.R., Whittaker, A.C., Bell, R.E., Watkins, S.E., Brooke, S.A.S., and Hann, M.G., 2020, New constraints on bedrock erodibility and landscape response times upstream of an active fault: Geomorphology, v. 351, p. 106937, doi:10.1016/j.geomorph.2019.106937.

APPENDICES

Appendix A

Table 1. Meadow Valley Wash knickpoint data. Location based on UTM Zone 11N.

X	Y	chi	elev
722615.8	4109926	3.347997	793.5527
713787.4	4099565	2.978644	764.8096
713333.2	4096130	4.170936	827.202
725653.2	4109103	5.154233	937.3061
716597.7	4105214	3.212575	768.7385
723467.4	4107258	4.171828	879.6506
716342.3	4112992	7.062883	1004.384
713418.4	4079694	3.57887	704.3134
727413.2	4115121	6.242884	945.142
714468.7	4100672	3.252622	756.5976
716115.2	4100729	5.331316	877.8942
717392.6	4100928	5.796121	910.4292
711658.4	4091759	4.419425	768.8367
705924.2	4093547	4.486887	796.2275
711686.8	4090311	5.192065	766.2946
716427.4	4110835	5.964961	942.2762
717449.4	4070922	5.041067	644.8868
713361.6	4099480	3.042045	750.5139
718329.4	4102688	6.386694	916.8176
726618.4	4110494	5.400067	936.3289
715320.3	4078218	3.630341	732.1533
706719	4097521	4.750516	826.391
715973.2	4106860	4.355268	851.6232
719408.1	4108138	5.508185	875.5299
714440.3	4107513	5.335216	914.373
715433.9	4076912	6.082476	716.2488
712850.6	4086990	7.119316	810.5032
713531.9	4102177	4.266023	816.4175
707712.6	4093746	4.296589	732.207
706548.7	4094711	6.688695	816.2451
711147.4	4098770	3.071221	747.9505
715320.3	4078956	4.802719	737.9791
713730.6	4103142	4.24956	783.4586
703681.6	4086450	6.822633	794.4573
715178.4	4077139	4.842064	718.3196
705839	4090027	4.959765	737.4758
706491.9	4081369	2.754564	639.9257
715802.9	4076060	6.051471	710.4733
711857.1	4085968	6.523077	781.3516
715916.5	4076799	6.286364	720.0142
706122.9	4082987	3.902649	677.1653
710125.5	4096187	4.841965	755.6232
705242.9	4078076	5.323819	703.547

Table 1 continued.

X	Y	chi	elev
706889.4	4084179	2.957146	640.7599
715888.1	4074868	5.470125	694.8545
711771.9	4094370	3.808033	733.0839
711715.2	4081170	6.384509	693.9492
724375.8	4063939	7.796224	621.0115
728974.5	4059738	5.202078	598.503
727044.2	4063485	3.660989	604.0028
727640.3	4062122	2.649011	597.3852
729315.2	4057410	4.344445	582.7513

Table 2. White River Valley knickpoint data. Location based on UTM Zone 11N.

X	Y	chi	elev
678928.1	4100303	2.680945	797.78
680602.9	4068566	4.172492	944.2207
679041.6	4074840	4.798706	938.0853
678104.8	4074357	5.171289	977.7519
677395.2	4081028	6.12336	975.6451
676231.3	4085371	6.894575	966.3086
686251.9	4056076	5.937859	828.9557
691617.1	4075720	3.508246	770.1712
689970.7	4099764	4.112175	874.825
678388.7	4094313	3.570841	789.5742
681170.7	4063088	8.541704	917.7747
682902.3	4054713	7.517023	888.4172
698231.3	4072058	5.349431	740.1167
700331.9	4072228	4.426197	708.3061
700019.7	4074499	6.811258	779.3747
695676.5	4070270	3.260162	647.4194

Table 3. Virgin River knickpoint data. Location based on UTM Zone 11N.

X	Y	chi	elev
799205.1	4103070	4.027137	750.4296
834890.8	4123667	7.03452	1041.425
867076.8	4123093	10.4305	1460.297
829669.9	4127396	7.033789	996.3881
858184	4128888	9.912486	1290.229
858499.6	4138039	11.40149	1529.813
841746.8	4130380	8.997847	1168.842
840943.6	4135830	11.27293	1354.529
813605.6	4096186	5.837472	950.3264
817908.5	4083707	7.972877	1298.632
812572.9	4076822	9.490148	1474.65
798057.6	4120856	7.131422	971.3765
798373.2	4125790	8.651456	1238.229
798918.2	4127712	9.425029	1363.321
807552.8	4124356	12.57554	1425.943
832079.5	4098394	6.580962	1272.876
797254.4	4081842	8.902892	1327.328
801672.1	4117442	7.19073	999.0954
803422	4124528	11.29503	1361.849
830415.7	4118188	7.714201	1152.831
838304.5	4113885	10.26728	1385.818
830214.9	4137982	8.680711	1217.69
847943	4125761	10.35759	1242.97
823990	4090276	7.194846	1132.163
765871.6	4108951	5.941087	852.3467
786353.6	4101751	7.520164	1141.427
746164.2	4049169	3.016521	614.7603
779784.5	4101693	8.6704	1071.482
824047.4	4127052	8.192132	1028.749
739250.8	4102439	5.832401	890.6832
759904.9	4115922	7.716642	977.6021
772612.9	4105537	8.740085	991.9136
805544.7	4116237	8.244417	954.3043
812601.6	4119680	9.730798	1037.017
820834.5	4116323	6.876839	900.3596
795762.7	4113197	8.384559	925.5446
823502.3	4116582	7.767603	987.2882
764638.1	4101923	6.029219	770.3072

Table 3 continued.

X	Y	chi	elev
780501.6	4096472	7.70225	844.7836
749147.5	4063770	5.98488	690.163
744701.2	4098853	5.469695	843.5311
766990.4	4080752	2.665157	563.636
746709.2	4088412	4.552283	727.6839
746336.3	4055595	8.492182	707.8702
746393.7	4062393	5.103932	640.4775
767592.8	4071114	4.844689	661.6269
767879.7	4075818	3.465951	557.2613
767306	4082043	3.712948	586.1438
769916.4	4083019	3.179608	564.8973
767678.9	4074872	3.446894	574.575

Table 4. Processed 10Be fluvial sand sample data.

Sample	Latitude	Longitude	ksn	Contributing Drainage Area	Erosion Rate mm/k.y	Mean Annual Precipitation (mm/yr)
MWV2	114.4739819	37.1596879	94.244320	5171132682	45.848	258
MWV3	114.4667947	37.2629058	86.973949	5004475393	44.697	258
MWV6	114.5726109	37.4495641	78.024699	4474185541	54.793	258
MWV4	114.136842	38.1579978	34.865408	2275335	19.604	258

Table 5. Raw unprocessed 10Be cosmogenic data from PRIME Lab for river sediment samples.

Nuclide Id	Sample Id	Aliquot Id	User Identification	Sample Mass (g)	Native Beryllium (mg)	^{9}Be Carrier (mg)	Average Current (nA)	Interference (Counts/Sec)	^{10}Be Ratio ($x10^{-15}$)	^{10}Be Std Dev ($x10^{-15}$)	Total ^{10}Be Atoms	Std Dev	Carrier-Corrected Total ^{10}Be Atoms	Carrier-Corrected Std Dev	Cosmogenic ^{10}Be Atoms per gram SiO_2	Std Dev	Relative Uncertainty (%)	Uncertainty in the AMS Measurement (%)
1	202302218	A	MVW2	18.460		0.2637	6027	0.3	233.1	6.8	4,107,633	120,339	4,104,530	120,422	222,347	6,523	2.9	2.9
1	202302219	A	MVW3	15.588		0.2639	6246	0.2	204.0	6.3	3,597,445	110,367	3,594,340	110,457	230,584	7,086	3.1	3.1
1	202302220	A	MVW4	31.286		0.2641	5531	0.6	1052	17	18,567,868	305,831	18,564,761	305,864	593,389	9,776	1.6	1.6
1	202302221	A	MVW6	19.940		0.2640	3809	0.2	216.9	10.1	3,826,992	178,327	3,823,886	178,383	191,770	8,946	4.7	4.7

Appendix B

MATLAB code for the knickpoint celerity model implemented with a 2-lithology grid search.

Modified from code used in (Zondervan et al., 2020).

```
clear

% Setting up 2D grid search
%Select a range of erodibility (Erosional efficientcy) values to test for the
two lithologies
L1_values = (0.1e-12:0.1e-12 :10e-12);
L2_values = (0.1e-12:0.1e-12 :10e-12);


%grid the two vectors
[L1,L2] = meshgrid(L1_values,L2_values)
% Ensure both L1_values and L2_values have the same length


c = 1; % initialize counter

% Load in profile csv
% csv should have 5 columns!
% 1: Downstream Distance, 2:Drainage Area, 3: Elevation,
% 4: Erosional efficientcy (set to zero),
% 5; Lithology along the profile either a 1 or 2
filename = 'F:\KP migration code\MVW_10M_2_liths.csv';
data = readtable(filename);


% Store data
LParams = nan(numel(L1_values) * numel(L2_values), 2);

% Create an array to store modeled Kickpoint Distance
KP_Distances = nan(size(LParams, 1), 1);

% Call the custom function using double nested loops
numL1 = numel(L1_values);
numL2 = numel(L2_values);
```

```
 %Initiate double nested loop

 for k = 1:numL1
     for j = 1:numL2
         % Call the custom function for each combination of L1 and L2
         Modified_values = data;

        % Set reference values with different ranges based on lithology
         lithologyValues = unique(data.Lithology);


         % Reset Modified_values to the original data for each simulation
         Modified_values = data;

         %Set up code to fill each interated L1 and L2 value into the data
         %based on if it is lithology 1 or 2


         % Set reference values
         keys = [1, 2];
         L1_vs = L1(k,j);
         L2_vs = L2(k,j);
         values = {L1_vs, L2_vs};
         referenceValues = containers.Map(keys, values);


         % Find rows where erosional efficiency is zero
         zeroEfficiencyRows = Modified_values.EE == 0;

         % Update erosional efficiency based on lithology for rows with zero
efficiency
         Modified_values.EE(zeroEfficiencyRows) = arrayfun(@(x)
referenceValues(x), Modified_values.Lithology(zeroEfficiencyRows));



 % Code modified from knickretreat model. (Zondervan et al., 2020)
 % Choose a value for precipitation in m/yr
 p = 0.258; % Average modern precipitation in caliente Nevada per year

 % Choose upstream distance of the knickpoint (m) and the time of initiation
(yr)
 knick = 116805; %upstream distance of 800m observed knickpoint in MVW
 knickage = 5600000;
```

```
 Downstream_dist = Modified_values.DD;
 Area = Modified_values.DA;
 Elev = Modified_values.Elev;
 Eff = Modified_values.EE;

 Lf = max(Downstream_dist); % m
 Lk = max(Downstream_dist); % m
 w2a = 0.001; % Channel width to drainage area scaling (optional, default)
(dimensionless)

 Psi = 10 * 1 * p * w2a;

 endLk = max(Downstream_dist) - knick; % m

 t = 0;
 ht = 10000; % yr

 [~, posLk] = min(abs(Downstream_dist - endLk));
 [~, posLf] = min(abs(Downstream_dist - Lf));

 %disp(['first estimate of the age of knickpoint ', num2str(knickage), ' yrs']);

 Areas = [];
 vlist = [0];
 Lk_lst = [Lk];
 t_lst = [t];

 for i = 1:floor(knickage / ht)
     X = min(abs(Downstream_dist - Lk)); % Equivalent to python version of
dclose (not index)
     A = repmat(Downstream_dist,[1 length(Lk)]) ;
     [minValue,LkIndex] = min(abs(A-Lk)) ; %LkIndex equivalent to index version
of dclose
     if X - Lk < 0
         A = ((Area(LkIndex + 1) - Area(LkIndex)) / (Downstream_dist(LkIndex +
1) - X)) * (Lk - X) + Area(LkIndex);
     else
         A = ((Area(LkIndex) - Area(LkIndex - 1)) / (X - Downstream_dist(LkIndex
- 1))) * (Lk - Downstream_dist(LkIndex - 1)) + Area(LkIndex - 1);
     end
     Ef = Eff(LkIndex);

     v = Psi * Ef * 365 * 3600 * 24 * sqrt(A) * 1000; % mm/yr
     vlist = [vlist, v];
     Lk = Lk - v * ht / 1000;
```

```
    Lk_lst = [Lk_lst, Lk];
    t = t + ht;
    t_lst = [t_lst, t];
    %Areas(i)=A;
 end
  KP_Distances(c) = Lk_lst(end); % Store the result
  LParams(c,:) = [L1_vs,L2_vs] ; %Store parameters used per model run

  c = c + 1; % Increment counter



    end
 end







 missfits = (endLk - KP_Distances)/1000; %calculate missfits from observed and
convert to kilometers

 figure;
 scatter(LParams(:,1),LParams(:,2),50,missfits,'filled')
 colorbar;
 grid on
 title("Missfit = observed - modeled")
 xlabel("Lithology 1 EE values")
 ylabel("Lithology 2 EE values")
 disp(Areas)
 n = [1:560] ;
 %plot(n,Areas)

 %save data to csv
 % Specify the full file path
 file_path = 'F:\KP migration code\2_param_grid_MVW_KP_distances_run9.csv';

 % Save the array to a CSV file at the specified location
 csvwrite(file_path, KP_Distances);
 % Specify the full file path
 file_path = 'F:\KP migration code\2_param_grid_MVW_Lparams_run9.csv';

 % Save the array to a CSV file at the specified location
 csvwrite(file_path, LParams);
```

Appendix C

Cosmogenic Sample Preparation Procedure
Physical Separation:

1. Break down sediment sample in a Jaw crusher.

2. Sieve samples to isolate grain sizes between 0.2 and 0.5 mm in diameter.

3. Re-crush samples too larger than 0.5mm in a disc mill pulverizer and re-sieve.

4. Send sieved samples to Purdue Rare Isotope Measurement Laboratory (PRIME Lab) for chemical processing.

Chemical Separation: (Purdue Rare Isotope Measurement Laboratory)

Rinse Fines:

1. Label a 4-liter beaker with the sample's name.

2. Pour ~500 milliliters of deionized water into the beaker.

3. Gradually add the sample, minimizing dust release.

4. Fill the beaker to two-thirds full with DI water, let larger particles settle, and decant the water.

5. Repeat until the decanted water is clear, up to 10 times.

Froth Flotation:

- For samples containing feldspar and mica, a carbonated solution is used to make feldspar and mica hydrophobic while keeping quartz hydrophilic.

- Freshly cracked grains of the correct size (0.25-0.5 mm) are essential to ensure separation efficiency.

- This process can separate up to 95% of feldspar, reducing the need for acid and time.

Aqua Regia:

1. Label a 4-liter beaker with "HCl/HNO3".

2. Add DI water to cover the sample.

3. Slowly add nitric acid, then hydrochloric acid, maintaining a 1:1 volume ratio.

4. Cover the beaker and let it sit overnight in a fume hood.

5. Repeat as necessary based on the sample's carbonate content.

Rinse and Dry:

1. Place the waste acid container in the fume hood.

2. Decant the acid from the beaker into the waste container.

3. Rinse the sample with DI water, decanting into the waste container each time until the water is clear.

4. Rinse thoroughly with DI water 15-20 times.

5. Transfer the sample to a 1-liter beaker and dry in the oven.

Magnetic Separation:

1. Perform magnetic separation either before or after roller leaching, based on sample quantity.

2. Pass the dried sample through a hand magnet and magnetic separator, collecting magnetic grains.

3. Clean the separator thoroughly.

4. Adjust settings to collect magnetic and non-magnetic grains separately.

5. Save non-magnetic grains, properly labeled.

Leaching:

1. Label and weigh High Density Polyethylene bottles for 5% HF/HNO3 solution.

2. Divide the sample equally among the bottles.

3. Add 0.75 liters of 5% hydrofluoric/nitric acid solution to each bottle.

4. Roll the bottles at a moderate heat setting overnight.

5. Rinse bottles multiple times, neutralize waste acid, and dry.

Refilling the Hydrofluoric Acid/Nitric Acid Carboy:

1. Refill the carboy at the end of each day to maintain a 5% acid solution.

2. Top off with pure water to the marked line.

Heavy Liquid Separation:

1. Use 250 mL separatory funnels and a dense liquid (LST) for mineral separation.

2. Allow sediment to settle, then drain the dense minerals through a coffee filter.

3. Repeat with additional water and shaking until separation is complete.

4. Rinse and save the dense minerals; prepare quartz for ultrasonic leaching.

Heavy Liquid Cleaning:

1. Filter and clean the heavy liquid for reuse, using a vacuum pump and hot plate.

2. Add hydrogen peroxide if the liquid becomes discolored.

Ultrasonic Leaching:

1. Ensure the ultrasonic tank is filled with enough water.

2. Fill Polypropylene bottles with 1% HF/HNO3 solution and place in the tank.

3. Operate overnight, then rinse samples thoroughly:

Acid Neutralization

- Use the WASTECH machine to safely neutralize waste acid before disposal.

ICPOES Analysis:

1. Prepare samples with HF/HNO3 solution.

2. Weigh 0.25 grams of clean quartz into a digestion bomb.

3. Dilute and analyze the sample using ICPOES.

Accelerator Mass Spectrometer (ams)

^{10}Be concentrations measured in the ams.